MICROFLUIDICALLY CRYO-COOLED PLANAR COILS

FOR MAGNETIC RESONANCE IMAGING

A Dissertation

by

CHIWAN KOO

Submitted to the Office of Graduate Studies of
Texas A&M University
in partial fulfillment of the requirements for the degree of

DOCTOR OF PHILOSOPHY

Chair of Committee,   Arum Han
Committee Members,   Steven M. Wright
                        Mary P. McDougall
                        Raffaella Righetti
Head of Department,   Gerald L. Cote

August 2013

Major Subject: Biomedical Engineering

ABSTRACT

High signal-to-noise ratio (SNR) is typically required for higher resolution and faster

speed in magnetic resonance imaging (MRI). Planar microcoils as receiver probes in

MRI systems offer the potential to be configured into array elements for fast imaging as

well as to enable the imaging of extremely small objects. Microcoils, however, are

thermal noise dominant and suffer limited SNR. Cryo-cooling for the microcoils can

reduce the thermal noise, however conventional cryostats are not optimum for the

microcoils because they typically use a thick vacuum gap to keep samples to be imaged

to near room temperature during cryo-cooling. This vacuum gap is typically larger than

the most sensitive region of the microcoils that defines the imaging depth, which is

approximately the same as the diameters of the microcoils.

Here microfluidic technology is utilized to locally cryo-cool the microcoils and

minimize the thermal isolation gap so that the imaging surface is within the imaging

depth of the microcoils. The first system consists of a planar microcoil with

microfluidically cryo-cooling channels, a thin N_2 gap and an imaging. The microcoil was

locally cryo-cooled while maintaining the sample above 8℃. MR images using a 4.7

Tesla MRI system shows an average SNR enhancement of 1.47 fold. Second, the system

has been further developed into a cryo-cooled microcoil system with inductive coupling

to cryo-cool both the microcoil and the on-chip microfabricated resonating capacitor to

further improve the Q improvement. Here inductive coupling was used to eliminate the

physical connection between the microcoil and the tuning network so that a single cryo-

cooling microfluidic channel could enclose both the microcoil and the capacitor with minimum loss in cooling capacity. Q improvement was 2.6 fold compared to a conventional microcoil with high-Q varactors and transmission line connection.

Microfluidically tunable capacitors with the 653% tunability and Q of 1.3 fold higher compared to a conventional varactor have been developed and demonstrated as matching/tuning networks as a proof of concept.

These developed microfluidically cryo-cooling system and tunable capacitors for improving SNR will potentially allow MR microcoils to have high-resolution images over small samples.

To my family for their love and support

ACKNOWLEDGEMENTS

I would like to thank my advisor, Dr. Han, for his support and guidance throughout my research and Ph.D. experiences. His knowledge, ideas, and commitment to the highest standards inspired and motivated me to think outside the box. I would also like to thank my committee members, Dr. Wright, Dr. McDougall, and Dr. Righetti, for their guidance and support throughout the course of this research.

I have received great help from my NanoBio Systems labmates and would especially like to thank Jaewon, Huijie, and Hyun Soo for their help and ideas pertaining to my research. I also want to extend my gratitude to Ke, Mario, Richard, and John. They worked with me closely to help me conduct my MRI experiments. Thanks also go out to Dr. Huff and his lab members, Mike and Shuli, for their help on the RF design and measurement. Also, thanks to Dr. Son and his lab member, Yerok, for ratiometric temperature image testing. I thank my friends, colleagues, and the department faculty and staff for making my time at Texas A&M University a great experience.

I would also like to thank my parents, sisters, and younger brother. They have always encouraged and supported me in my research. Most of all, I would like to thank my wife, Juhee. None of this would have been possible without her endless love and sacrifice. This thesis is dedicated to my parents, wife and my lovely children who have always stood by me.

TABLE OF CONTENTS

Page

LIST OF FIGURES

LIST OF TABLES

CHAPTER I

INTRODUCTION

1.1. Magnetic Resonance Imaging (MRI) and Signal to Noise Ratio (SNR)

Magnetic resonance imaging (MRI) is generally considered to be a signal-to-noise ratio (SNR) limited technique, particularly in the case of MR microscopy [1, 2]. As the signal-to-noise ratio is proportional to the number of spins in a given voxel, all other parameters remaining constant, decreasing a voxel size by a factor of 10 in each direction results in a decrease in SNR of a factor of 1000. Recovering the SNR loss through signal averaging is impractical, as the noise only decreases as the square root of the number of averages, meaning that one million averages would be required to maintain the same SNR as obtained when the resolution was a factor of 10 poorer.

SNR can be enhanced by other means, such as using higher magnetic field strengths, or in some cases through clever sequence design, but in general one must reduce the size of the coil to recover some SNR. When using very small coils, or alternatively larger coils with very small samples, it readily becomes apparent that the dominant noise source is the thermal noise generated by the resistance in the coil conductor. Therefore, to improve SNR, several efforts have been made to reduce the noise of MR coils using liquid nitrogen cryo-cooling or superconducting materials for MR coils, where SNR improvement of 2-3 fold was reported [1, 3-6]. However, due to the large size of conventional cryostats and the requirement to keep the sample at near-room temperature, the distance between receiver coils and samples often increases in

cryo-cooled coils, resulting in degradation of the achievable SNR of the coil. It is generally accepted that the most useful region of sensitivity for a coil exists within approximately one coil width above it; therefore, this increased coil to sample distance has also limited the use of cryo-cooling to coils with larger dimensions [4, 6], such that a cryostat several millimeters thick does not reduce the effectiveness of the coil.

McDougall *et al.* have been investigating the use of coils that are small in one dimension (2 mm wide and up to 80 mm long) as array elements for parallel imaging [7, 8]. Using 64-channel arrays of these elements, they have demonstrated imaging in a plane parallel to the array in a single echo- a technique appropriately called "Single-Echo Acquisition" imaging, or SEA imaging [9, 10]. As with conventional small coils, the dominant noise source in the receiver coils (array elements) is the thermal noise of the copper. Even though the coils are long in one direction, they are very narrow (the imaging voxel width in the case of SEA imaging) in the second direction, and thus have a relatively shallow sensitive region. The application of cryogenic cooling is obviously of interest to improve the available SNR, but the cryostat must eventually cover an entire array to work with SEA imaging. Because even a small increase in the distance between the coil and a target sample can significantly degrade the achievable SNR of the 2 mm wide coil, a cryo-cooling system that significantly increases the distance between the SEA coils and the sample cannot be used.

1.2. Microfluidic Cooling System

The use of microfluidics has seen a huge surge in varieties of applications during the past decade. One important microfluidic application is in cooling, mainly for electrical circuits and components. Increased power consumption of more advanced and complex systems coupled with smaller system size causes serious thermal management issues and the systems must be managed through proper cooling [11]. Many efforts have focused on developing miniaturized fluidic systems that can drive liquid-phase coolants through micrometer-scale fluidic channels [12-15]. The high surface to volume ratio of microfluidic channels enhances heat dissipation through the coolant.

Although these miniaturized liquid cooling systems show significantly higher cooling efficiency over conventional systems, their main applications are for cooling heated electronic components or systems down to room temperature. This is different from cryogenic cooling systems which are mainly used to cool components down to liquid nitrogen temperature for improved sensitivity and low noise. There have been reports of developing micropumps for compact cryogenic cooling system for high-temperature superconducting systems or charged-coupled devices [16, 17], but those systems are not applicable to cryo-cool small MR coils.

Here, a microfluidic cryo-cooling system has been designed for integration with miniature MR coils such as described above. Two features in particular allow for close placement of the cryo-cooled coil and the sample. First, the system consists of a microfluidic channel placed directly underneath the coil, through which liquid nitrogen is pumped, cryo-cooling the coil to liquid nitrogen temperature in a very localized

manner. When liquid nitrogen flows through a micrometer scale fluidic channel, the microliter volume of liquid nitrogen is minute compared to a fluidic channel used in conventional cryostats. Due to the small heat capacity associated with the small volume of the microchannel, only the area directly adjacent to the microchannel, in this case the coils, will be cooled down to liquid nitrogen temperature. Secondly, by separating the imaging surface from the cryo-cooled coil by a thin air gap and flowing nitrogen gas through the gap, the convection heat transfer to the imaging surface is minimized, effectively preventing the sample from freezing.

CHAPTER II

SINGLE MICROFLUIDICALLY CRYO-COOLED MAGNETIC RESONANCE (MR)

PLANAR PAIR COIL *

2.1. Introduction

In general, the SNR of a microcoil (coil-loss dominated) is proportional to the square root of Q. Thus if the resistance of the microcoil is decreased with better components or conductors, without changing the coil configuration or distance to the sample, the SNR will be improved. However, when cryo-cooling, SNR is proportional to both the square root of temperature (in the cooled portion) and the square root of overall resistance. Theoretically, the SNR gain by cooling a copper coil can be predicted using the following equation [4, 6]:

$$\text{SNR}_{\text{improvement}} = \sqrt{\frac{R_{\text{unload,room}}T_{\text{room}} + R_{\text{sample}}T_{\text{sample}}}{R_{\text{unload,cooled}}T_{\text{cooled}} + R_{\text{sample}}T_{\text{sample}}}} \tag{1}$$

R_{unload} is the resistance of the coil itself without sample loading and R_{sample} represents the resistance added by the sample. If the temperature of the coil decreases from room temperature (T_{room} = 27℃ (300K)) to liquid nitrogen (LN) temperature (T_{cooled} = -196℃ (77K)), the resistivity of copper coils drops by a factor of eight [18]. However, because the skin depth is proportional to the square root of resistivity, the high frequency resistance of the coil at 27℃ decreases by a factor of $\sqrt{8}$ (= 2.83) at -196℃. Thus, from equation (1), the highest SNR improvement possible when cryo-cooling a copper-loss-dominated coil is 3.32, when R_{sample} = 0.

From equation (1), the following Q related SNR improvement equation can be extracted since inductance and frequency were held constant and $Q = \omega_0 L/R$:

$$SNR_{improvement}$$

$$= \sqrt{\frac{T_{room}/Q_{unload,room} + T_{sample}/Q_{sample}}{T_{cooled}/Q_{unload,cooled} + T_{sample}/Q_{sample}}} \tag{2}$$

The design concept was to locally cryo-cool the MR coil with microfluidic channels carrying liquid nitrogen while simultaneously minimizing the distance between the coil and the imaging surface for maximum SNR, maintaining the temperature of the imaging surface above the water freezing temperature, and maintaining minimal liquid nitrogen consumption.

2.2. Design

The device consists of a cryo-cooling microfluidic channel through which liquid nitrogen can flow, integrated with a 2 mm wide by 57 mm long planar RF coil and an imaging surface on which target samples to be imaged can be placed (Figure 1a).

Poly(dimethylsiloxane) (PDMS, thermal conductivity = 0.18 W/mK) was used as the microchannel material. Since only a small amount of liquid nitrogen was carried through the micrometer-scale channel, only areas directly adjacent to this channel were cooled to liquid nitrogen temperature. The fluidic channel cryo-cooled only the main coil element and not the RF components used for matching and tuning the coil (Figure 1b, c). Further SNR improvement could be achieved by cryo-cooling the RF components, but this would require a larger channel to cover the RF components and a large cryostat, and was outside the scope of this study. The cryo-cooling microfluidic channel was 30 µm deep and 2 mm wide to cover the planar coil width.

The coil was fabricated on a 0.5 mm thick poly(methyl methacrylate) (PMMA) substrate using microfabrication. Since the PMMA material has lower thermal conductivity (0.17 W/mK) than silicon (1.6 W/mK) or glass (1.1 W/mK), it reduces the heat flux between the liquid nitrogen channel and the nitrogen gap. The coil was a standard planar pair design [19], consisting of three copper traces, each being 0.25 mm wide with 0.5 mm spacing between them. The overall length of the coil was 57 mm. This design was based on our previous design of a 64 element array of planar pair coils for highly accelerated SEA MR imaging [9]. To bond the planar coil substrate and the cryo-

7

cooling microfluidic channel layer, a 0.1 mm thick spin-coated PDMS adhesion layer was used.

The imaging surface was 0.6 mm thick and was separated from the coil by a 1.0 mm thick nitrogen gap and supported by two vertical side support structures. This flowing nitrogen gap reduced direct thermal conduction between the cryo-cooled coil substrate and the imaging surface, preventing samples from freezing during MR image acquisition.
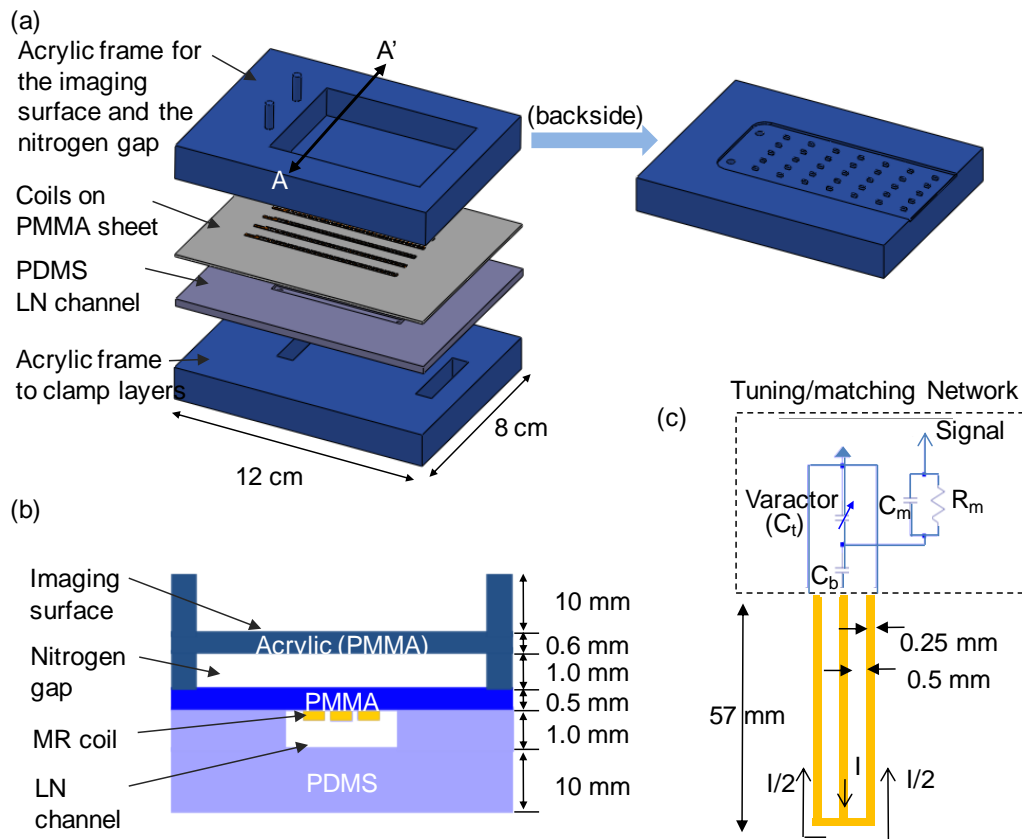
Figure 1. Schematic diagrams of the microfluidically cryo-cooled MR planar coil device. (a) Illustration of each layer of the device. (b) Cross sectional view (A-A') of the device. (c) Design of the planar pair coil and a typical tuning/matching network (C_m: matching capacitor, C_t: tuning varactor, and C_b: DC blocking capacitor), with current paths indicated.

2.3. Thermal Simulation

To predict the temperature of the coil and the imaging surface of the integrated cryo-cooling structure during operation, finite element method (FEM)-based models were implemented using commercially available FEM software (Comsol Multiphysics^{TM}, COMSOL Inc., Los Angeles, CA). Thermal conductivity parameters of 400 W/mK, 0.18 W/mK, and 0.17 W/mK were selected for copper, PDMS, and PMMA, respectively. Room temperature (300 K) was used as the initial temperature of the structure and the surrounding.

It was assumed that heat conduction and convection are negligible in the nitrogen gap area while nitrogen gas is flowing continuously; therefore the nitrogen area was left as a blank space. The imaging surface temperature was also simulated for varying microchannel widths, from 0.76 mm (3 times the width of the coil trace) to 2790 μm (11 times the width of the coil trace), and varying heights (0.03 mm to 1 mm). Finally, the effect of the nitrogen gap height (varying from 0.5 mm to 1.0 mm) on the imaging surface temperature was simulated.

Figure 2 shows the simulation result. The cryo-cooling microchannel directly covers the planar coil through a 100 μm thick protective polymer layer (PDMS). As a result of this near-direct contact, the simulation result showed the coil temperature to be -194℃, almost identical to the liquid nitrogen temperature of -196℃. The temperature of the imaging surface during cryo-cooling was maintained at around 17℃. The temperature decreased to 2℃, however, when the nitrogen gap depth was reduced from 1.0 mm to 0.5 mm. A nitrogen gap depth of larger than 1.0 mm was not suitable since

9

that would put the phantom outside the optimal imaging depth of the planar pair coil.
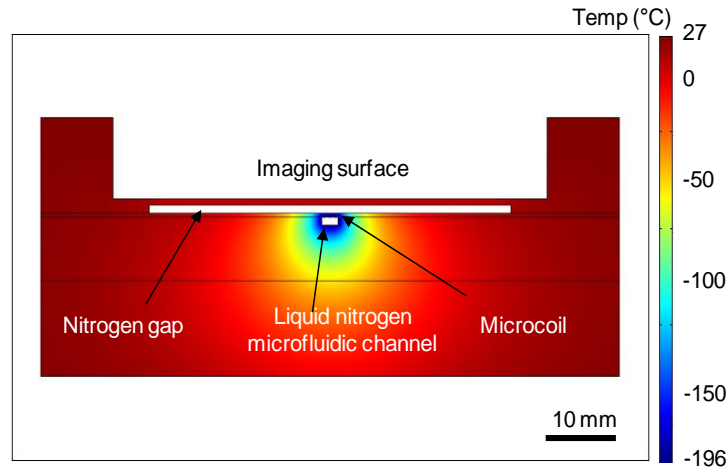
Figure 2. FEM simulation result of the device temperature profile when liquid nitrogen flows through the microfluidic channel. Temperature at the coil was almost identical as the liquid nitrogen temperature (-196℃), and the temperature of the imaging surface was maintained above the water freezing temperature of 0℃ when the nitrogen gap was 1.0 mm.

When increasing the cryo-cooling microchannel width from 2 mm to 3 mm, the imaging surface temperature dropped by 9℃. When varying the height from 30 µm to 1 mm while maintaining the width of the microchannel at 2 mm, the imaging surface temperature dropped only slightly by 7℃. Thus, it appears that the imaging surface temperature depended on the cryo-cooling channel width more than on the the height. Simulations showed that no special heat sink apparatus was required for our device because the cold temperature is very localized right around the liquid nitrogen flowing microfluidic channel due to the small heat capacity of the microchannel.

2.4. Fabrication and Assembly

The overall fabrication steps are illustrated in Figure 3. A thin PMMA substrate was prepared first. The 0.5 mm thick substrate was made from the 1.6 mm thick PMMA sheet (Regal Plastics, Austin, TX) using a hot press (Manual hydraulic 15 ton press, Specac Inc., Cranstron, RI).   Next, chromium and copper films (25 nm / 300 nm) were deposited on the PMMA substrates using an electron-beam evaporator. The chromium layer functioned as an adhesion layer for copper. The 0.5 mm thick metal-coated PMMA substrate was then attached to a 1.6 mm thick PMMA sheet using Kapton® tape to prevent the 0.5 mm thick PMMA substrate from bending during the subsequent photolithography process. To define the planar coils, a 45 µm thick negative photoresist layer (NR2-20000P, Futurrex, Inc., Franklin, NJ) was spun on the substrate at 500 rpm for 10 s followed by spinning at 2800 rpm for 30 s. The substrate was then soft-baked at 80°C on a hot plate for 30 min and exposed under UV light using a mask aligner (1800 mJ/cm2, MA-6, Suss MicroTec Inc., WaterBury, VT). A post exposure bake step at 80°C for 5 min was conducted, and the photoresist was developed in a developer (RD6, Futurrex, Inc., Franklin, NJ) for 1.5 min. This developer is a water-based developer and does not affect the PMMA substrate while developing.

Following photolithography, copper electroplating was carried out in a copper sulfate solution ($CuSO_4$: H_2SO_4 : H_2O = 250 g : 25 ml : 1 L) at a current density of 10 mA/cm2 for two hours using a DC pulsed power supply (DUPR 10-1-03, Dynatronix Inc., Amery, WI) to obtain a 25 µm thick copper layer. Photoresist remover (RR4, Futurrex, Inc., Franklin, NJ) was used to remove the photoresist instead of commonly

used acetone to prevent the PMMA substrate from being damaged by the solvent. The 1.6 mm thick PMMA backing was detached, and the copper and chromium film was etched by copper etchant (CE-100, Transene Company Inc., Danvers, MA) and chrome etchant (TFE, Transene Company Inc., Danvers, MA). The coil fabricated substrate was rinsed by deionized water and dried with nitrogen blow. Finally, PDMS (10:1 mixture of Sylgard 184 silicone elastomer base and curing agent, Dow Corning., Midland, MI) was spun to a thickness of 100 µm at a spin speed of 3000 rpm for 30 s and cured at 85℃ for 30 min. This PDMS layer works as an adhesive layer to the PDMS cryo-cooling microfluidic channel and prevents the planar coil from lifting off from the PMMA substrate during the extreme temperature cycle between liquid nitrogen temperature and room temperature.

Next, the cryo-cooling microfluidic channel for liquid nitrogen delivery was fabricated in PDMS using soft lithography [20]. The master mold was fabricated in SU-8TM (MicroChem, Newton, MA) on a silicon wafer. PDMS pre-polymer mixture was then casted onto the master mold and degassed in a vacuum desiccator (Bel-Art Products, Pequannock, NJ) for 30 min to remove bubbles trapped inside the PDMS mixture, followed by curing in an 85℃ oven for one hour. After releasing the polymerized PDMS replica from the master mold, this PDMS cryo-cooling microfluidic channel and the previously fabricated PDMS coated planar coils were bonded together after oxygen plasma treatment [21, 22] with an O_2 plasma chamber (Harrick Plasma, Ithaca, NY).
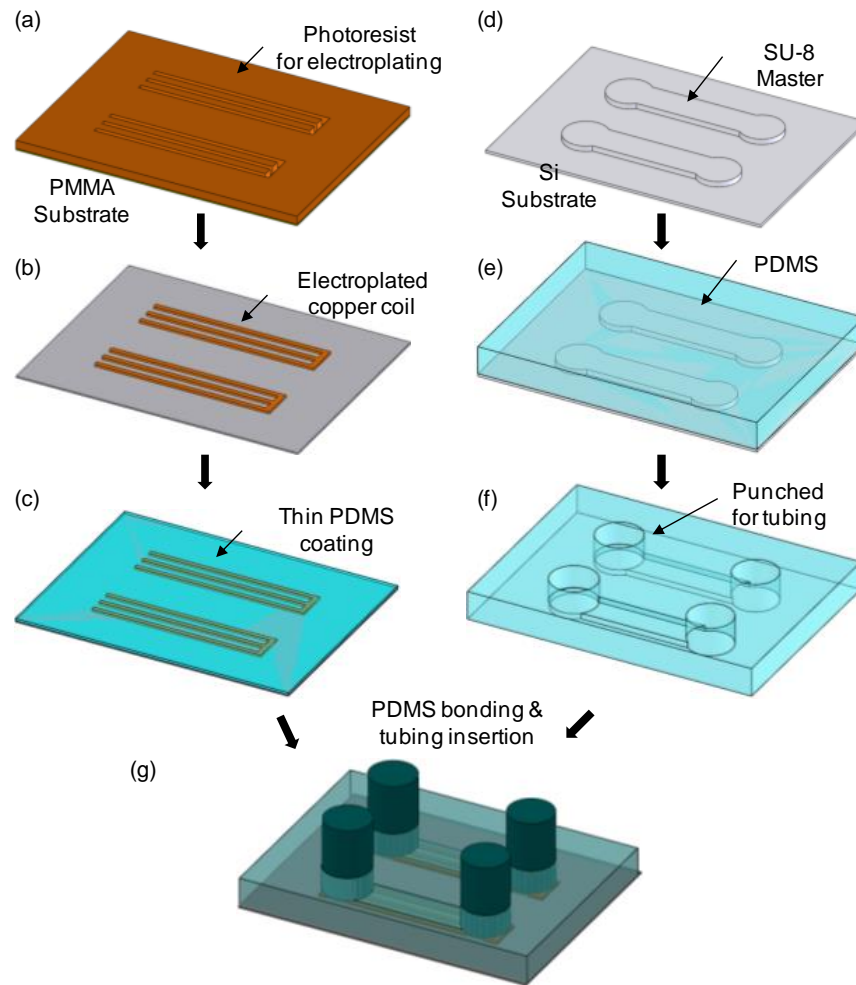
Figure 3. Fabrication steps for the MR planar coil layer (a-c), the cryo-cooling microfluidic channel layer (d-f), and the final assembly and tubing insertion (g). (a) Negative photoresist (NR2-20000P) patterning on a thin PMMA substrate with Cr/Cu as seed layers. (b) Cu electroplating to 25 µm height and removal of the photoresist and Cr/Cu seed layers. (c) Thin PDMS coating. (d) SU-8 mold fabrication on Si substrate. (e) PDMS casting on the master mold for liquid nitrogen channel layer fabrication. (f) PDMS channel layer releasing and hole punching for tubing insertion. (g) Bonding between the MR planar coil layer and the PDMS liquid nitrogen channel, and inlet/outlet tubing insertion.

13

For fluidic interconnects, 3.18 mm outer diameter (OD) silicone tubing (Helix Medical, Carpinteria, CA) was chosen. After punching an inlet and an outlet hole through the PDMS cryo-cooling channel using a biopsy tool (Acuderm, Inc., Fort Lauderdale, FL), the 3.18 mm OD tubes were inserted into the holes. Following tubing insertion, uncured PDMS was applied on the top surface of the channel layer and cured to hold the inserted tubing tightly.

For coil matching and tuning, a separate PCB was fabricated on standard FR-4. The match/tune board contained the matching capacitor, a varactor diode (Microsemi, Irvine, CA) biased over the RF line in order to allow for adjustment from outside the bore without moving the system, a chip resistor in parallel with the matching capacitor to prevent DC blocking to the tuning varactor diode, and coaxial connection. The match/tune PCB was soldered directly to the end of the planar pair. In this initial design, the match/tune PCB could not be cryo-cooled by the cryo-cooling microfluidic channel due to its separate position.

Next, the nitrogen gap and an imaging surface were created in an acrylic block (80 × 210 × 12.5 mm, McMaster-Carr, Atlanta, GA) using a rapid prototyping machine (MDX-40, Roland DGA Corp., Irvine, CA). On the inner surface of the nitrogen gap, a small pillar array (1 mm in width, 2 mm in length, and same height as the nitrogen gap) was fabricated to prevent the gap from being collapsed under an external clamping force after the final assembly. Another acrylic board was prepared to support the liquid nitrogen tubing and nitrogen gas tubing. Semi-circle cradles were attached to the acrylic board using epoxy (Loctite, Henkel Corp., Cleveland, OH), fitted to the inside shape of

the acrylic cylinder which formed the inner surface of a conventional in-house designed bird-cage type volume coil that will be used in MR image tests.

For the final assembly step, the planar coil substrate bonded with the cryo-cooling microfluidic channel was attached to the acrylic frame using Kapton® tape to form the closed nitrogen gap channel. A second acrylic frame was used to clamp this sandwich structure using nylon screws. After the final assembly, the distance between the coil and the top of the imaging surface was 2.1 mm.

Figure 4 shows top and bottom views of the completely assembled cryo-cooled coil system. An initial liquid nitrogen flow test with the 30 µm high microfluidic channel resulted in only gas phase flowing from the outlet of the microchannel due to the high fluidic resistance of the microchannel. Since our simulation results showed that the height of the microfluidic cryo-cooling channel mainly does not affect the localized cooling capability and the temperature at the imaging surface, the channel height was increased to 1 mm.
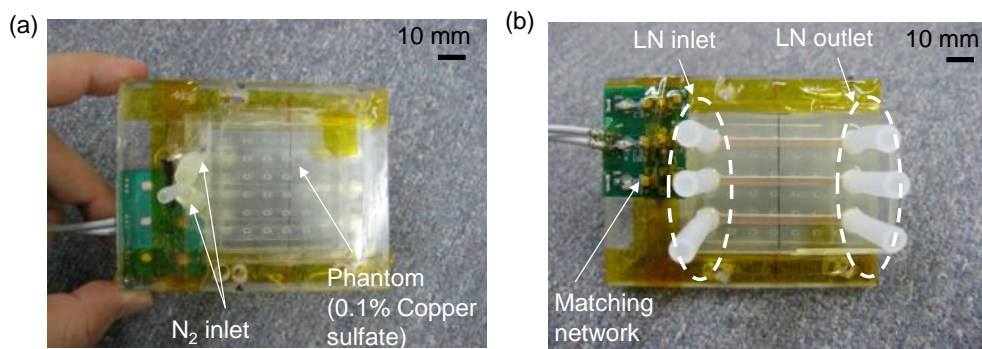
Figure 4. The fully assembled microfluidically cryo-cooled MR coil device. (a) Top and (b) bottom view of the assembled device.

2.5. Liquid Nitrogen Supply

To supply liquid nitrogen through the microfluidic channel, a 20 L dewar (Lab20 with withdrawal, Chart Industries, Inc., Garfield Heights, OH) was connected with 6.35 mm OD polyethylene tubing (VWR, West Chester, PA), which was then connected with 3.18 mm OD silicone tubing inserted into the PDMS cryo-cooling channel. The maximum pressure achievable with the dewar having the withdrawal apparatus is 34 KPa. To further increase the internal pressure of the dewar for faster liquid nitrogen pumping, nitrogen gas was pumped continuously during the course of the experiment into the dewar through a 6.35 mm OD polyethylene tubing. A driving pressure of 45 kPa resulted in liquid-phase nitrogen flowing from the outlet of the PDMS fluidic channel. Using this setup, liquid nitrogen flowed through the system for 60 minutes without any difficulties.

2.6. Temperature Characterization

While liquid nitrogen flows through the PDMS cryo-cooling channel, the imaging surface temperature and the PDMS channel layer surface temperature were characterized.

To characterize the surface temperature of the PDMS LN channel, luminescence thermometry using Mn-doped CdZ-ZnS core-shell nanocrystals was used. The nanocrystals exhibit strong temperature dependence of the spectral line shape while being insensitive to the surrounding chemical environment [23]. Ratiometric thermometry on the Mn luminescence spectrum was conducted to measure the temperature gradient around the PDMS LN channel (Figure 5a). A thin layer of Mn-doped nanocrystals from Park *et al.* [23] was spin-coated on a glass substrate (2×3 glass

16

slide, VWR, West Chester, PA). A PDMS thin layer (15 µm) was spin-coated on the nanoscrystals-coated glass and cured. The PDMS LN channel was made of black PDMS Sylgard 170, Dow Corning, Midland, MI) to minimize the light scatter and light noise. Black PDMS was casted on the master mold fabricated a 3D printer (ULTRA, envisionTEC, Dearborn, MI) for the LN channel ($3 \times 3 \times 10$ mm^3, $w \times h \times l$) and cured in an oven at 80℃ for 1 hour. Then, the black PDMS was released and permanently bonded to the nanocrystals-coated glass substrate. The PDMS LN channel device was placed in the enclosure made of black acetal resin blocks (McMaster-Carr, Atalanta, GA). The enclosure has an inlet and outlet tubing for supplying dry nitrogen gas to prevent frosting on the glass substrate while maintaining the temperature gradient on the glass substrate between ambient temperature to liquid nitrogen temperature. Figure 5b shows the illustration of the measurement setup. A 365 nm UV LED was used to excite the nanocrystals-coated glass substrate and a 475 nm pass filter was placed in front of the LED. Then a dichroic mirror (DMLP505R, Thorlabs, Newton, NJ) was placed to reflect the light from the LED to the glass substrate and to collect the emitted light from the nanocrystals on the glass substrate. Two bandpass filters for two intensity images at 600 and 650 nm were used in front of a CCD camera (PI-LCX, Princeton Instrument Trenton, NJ) and each intensity image at 600 and 650 nm was obtained using 20 s integration time. The intensity ratio between 600 and 650 nm was converted to temperature profile.
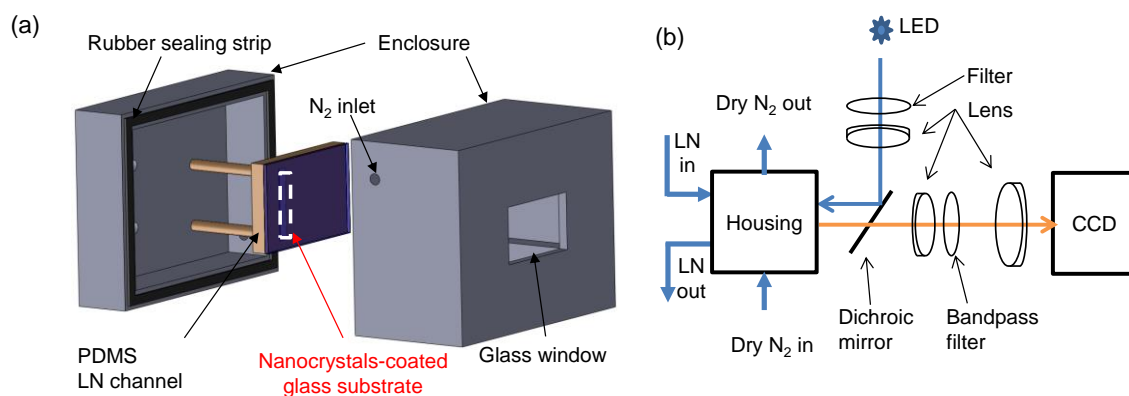
Figure 5. Schematics of the LN channel, the enclosure and the temperature measurement setup. (a) The LN device is in the enclosure in which dry nitrogen is constantly flushed. (b) The optical setup consists of filters, achromatic doublet lenses, and a dichroic mirror. The device was illuminated with a 365 nm LED and imaged with a CCD detector.

The surface temperature gradient around the LN channel was measured using the ratiometric thermometry with Mn-doped nanocrystals. Figure 6a shows the LN channel device and the imaging area. Figure 6b,c shows that the color contour plot of the emitted light intensity (at 650 nm) from the nanocrystals on the glass substrate and the temperature profile converted from the ratio of the intensity at 600 and 650 nm, respectively. The temperature inside the LN channel is close to liquid nitrogen temperature (77K, -196℃) and the temperature increased gradually up to 293K (20℃) over the distance of 12 mm due to the constant flush of dry nitrogen gas at 293K. This measurement matched well with the simulation result (Figure 6d). This measurement result verified that locally cryo-cooling using the LN microfluidic channel is possible.

18
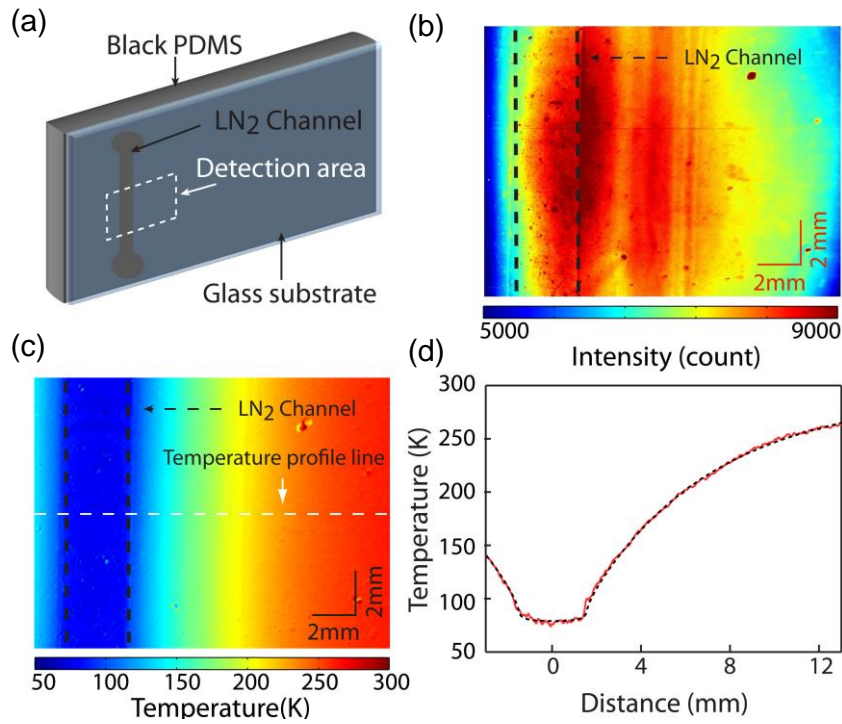
Figure 6. (a) Schematics of the PDMS LN channel device. The imaging area is indicated by the dashed rectangle. (b) Color contour plot of the intensity image (at 650 nm) from the device when flowing liquid nitrogen flow through the LN channel. (c) Color contour plot of the temperature converted from the intensity ratio image. (d) Temperature line profile (solid, red) and the simulation result (dashed, black) at the location indicated in (c)

Next, the effect of the nitrogen gap on the imaging surface temperature was characterized using a digital thermometer (HH508, Omega Engineering, Inc., Stamford, CT) and a K-type thermocouple probe (SC-GG-K-30-36, Omega Engineering, Inc., Stamford, CT) having a temperature measurement range of -200℃ to 1372℃. Nitrogen gap structures with gap depths of 0.5 and 1.0 mm used for simulations were prepared. Nitrogen gas at 70 KPa of pressure was constantly flowed through the nitrogen gap while the planar coil was being cooled using liquid nitrogen. The surface temperature was then measured every 30 seconds for 20 minutes using the digital thermometer. The

effect of the nitrogen gas pressure on the imaging surface temperature was also characterized. Three pressure setpoints (35, 70 and 97 KPa) were tested with the nitrogen gap structure having gap depth of 1.0 mm and the temperature on the imaging surface was measured every five minutes for one hour.

The 1.0 mm nitrogen gap structure was found to keep the imaging surface temperature at 6.5 ± 1.5℃ whereas the 0.5 mm nitrogen gap structure caused the imaging surface temperature to fall to -29 ± 7℃ (Figure 7a). These results show that the deeper nitrogen gap structure greatly reduced the cooling effect of the coil substrate on the imaging surface.

Figure 7b shows that by applying a higher nitrogen gas pressure to the nitrogen gap, the temperature drop at the imaging surface could be reduced. This is due to the reduced heat convection from the coil to the imaging surface. A pressure of 70 KPa was determined to be sufficient to thermally insulate the imaging surface from the liquid nitrogen channel while minimizing nitrogen gas consumption. In this condition, the temperature of the imaging surface was kept at approximately 8.0℃. This measured result matched well with the FEM simulation result.

To assess the temperature gradient along the long axis of the coil, the coil substrate temperature (backside of the coil) was measured using a thermocouple. This data is shown in Table 1. After 10 minutes of cryo-cooling, the inlet and outlet region temperatures converged and then readched below -190℃ after 20 minutes. There was no temperature gradient along the coil axis.
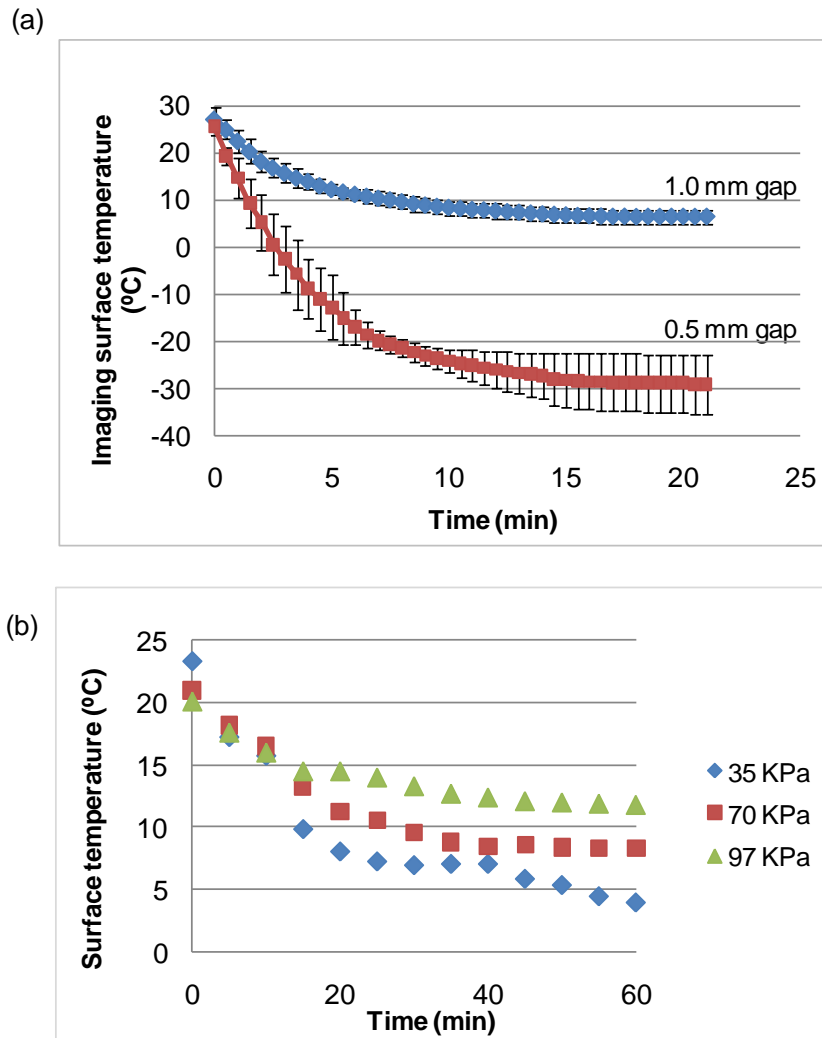
Figure 7. Imaging surface temperatures at two different nitrogen gap heights and at three different N_2 gas pressure. (a) 0.5 mm and 1.0 mm high gap at 70 KPa of N_2 gas pressure (n=3), and (b) 35, 70, and 97 KPa N_2 gas pressure with a 1.0 mm high gap.

Table 1. Temperature on the backside of the coil after cryo-cooling.

Time (min)	Temperature near the inlet (°C)	Temperature near the outlet (°C)
0	21.9	21.9
5	-111.1	-143
10	-181	-177.7
15	-191	-188
20	-192	-190
25	-191	-193.2
30	-192	-193

2.7. MR Coil Quality Factor (Q) Characterization

The loaded Q factors were measured with an S_{11} measurement using a network analyzer (HP4195A, Agilent Technologies, Santa Clara, CA). With the coil tuned to 200 MHz and matched to 50 ohm with 30dB return loss or better, the bandwidth Δf between the 7dB return loss points was measured. The Q values are calculated as $Q = f_0 / \Delta f$. This is different from the 3dB bandwidth used for standalone resonant circuits [24] due to the additional losses caused by matching the resonant circuit to the network analyzer.

When the coil was cryo-cooled using the microfluidic cryo-cooling channel, Q increased by a factor of 1.78 ± 0.08 ($n = 3$) compared to the coil at room temperature. The matching network was bulky so that the cryo-cooling channel could not cover them to cryo-cool. When the coil and the matching network were cryo-cooled by immersing

them into a liquid nitrogen bath, Q increased by a factor of 2.59 ± 0.06 (*n = 6*). This shows the effects of the resistance of the matching network which was not cryo-cooled at liquid nitrogen temperature.

2.8. SNR Improvement Characterization through MR Imaging

To compare the SNRs of the planar coil at room temperature and cryo-cooled temperature, initially two separate coils were prepared, one for room temperature (RT) characterization and the other for liquid nitrogen temperature (LT) characterization. This approach straightforwardly eliminated the issues associated with re-matching and tuning over the large range associated with cooled and uncooled copper. First, to find out the required capacitance, a tunable capacitor was used and the coil was matched to 50 ohm at room temperature and cryo-cooled temperature. The capacitance required at the two temperatures was measured, and then equal valued fixed chip capacitors were soldered on two circuits on a PCB board connected with the two coils respectively. A varactor diode was added in parallel with the tuning chip capacitor for fine-tuning from the outside of the magnet. The distance between the phantom and each coil were the same because the two coils were fabricated on the same substrate, thus enabling comparison of the SNRs of the two coils at two different temperatures (RT and LT).

For the test with a single coil for both room temperature and liquid nitrogen temperature MR imaging, another matching network using dual varactor diodes was fabricated. Here, one varactor diode was added across the matching capacitor and the other one to the tuning capacitor. Using two varactors enabled a single coil to be tuned

and matched at both room and cryo-cooled temperatures, eliminating any possible effects of different positions of two separate coils in the magnet field.

To evaluate the SNR of the coil, images of a phantom were obtained at both room and cryo-cooled temperature in a 4.7 Tesla magnet system (40 cm bore, Unity/Inova console, Varian, Palo Alto, CA). Figure 8 shows the schematic of the MR imaging test setup. To load the integrated coil system to the center of the magnet, a 90 cm long acrylic board and cradle were prepared. To supply liquid nitrogen from outside of the magnet to the cryo-cooled coil system, 1.2 m long 6.35 mm outer diameter (OD) polyethylene tubings wrapped around with insulating sponge foam tapes (Frost King, Mahwah, NJ) were fixed under the long acrylic board and were connected with the interface of the cryo-cooling channel using plastic tapered connectors.

The board was inserted into the acrylic cylinder having the volume coil and carefully affixed to prevent any movement due to contractions when the cryogens were applied. Next, the assembly was positioned inside the magnet for imaging. A liquid nitrogen dewar and a nitrogen gas cylinder were connected with the coil system (Figure 8c), with the liquid nitrogen Dewar located within the RF screen room for proximity to the coil system.

RT MR images of a phantom (0.1% copper sulfate solution, 1 g copper sulfate per 1 L water) were acquired in the axial plane (perpendicular to the imaging surface and the long axis of the coil) at the magnet isocenter. All images used a spin echo sequence with a matrix size of 256×256, TR (repetition time) of 500 ms, TE (echo time) of 50 ms, 2 averages, slice thickness of 3 mm, and spectral width of 20 kHz. Then, LT images

were obtained after flowing liquid nitrogen to the planar coil for 30–40 min and verifying that liquid phase nitrogen was flowing from the outlet LN tubing. To prevent ice formation around the match/tune PCB from leading to unstable tuning during MR image acquisition, an extra 3.18 mm OD tube was used to direct nitrogen gas at the RF components. Once cooled, the DC bias voltages to the varactors were adjusted to match and tune the cryo-cooled coil. Phantom images were obtained with the same parameters used for the RT imaging test.
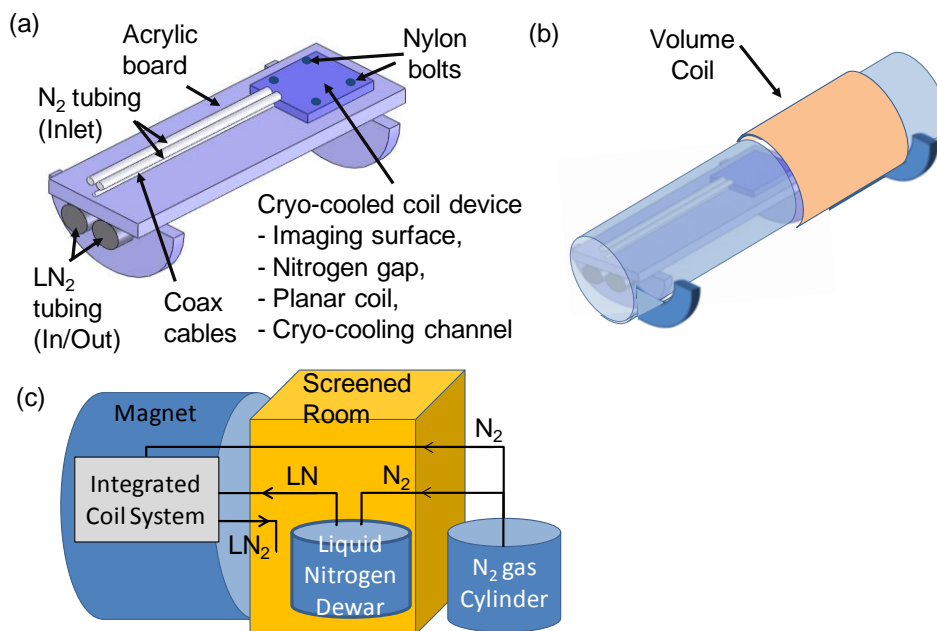
Figure 8. Schematics of the MR image acquisition experiment setup using the microfluidic cryo-cooled planar coil system. (a) The integrated cryo-cooled planar coil system on an acrylic board. (b) The coil system inserted into the volume coil and ready to be loaded into an MR magnet. (c) Nitrogen gas was used to drive liquid nitrogen out from the dewar as well as for flowing through the nitrogen gap of the surface coil system for temperature insulation.

MATLAB® was used to display images and to evaluate the SNR. First, 2D Fourier transform was used to reconstruct the magnitude image (256 × 256 matrix) without any correction filter. Then, the signal magnitude matrix was divided by the average of the noise value in one large noise regions to obtain an SNR matrix. The SNR profile along a line going through the maximum point of the SNR matrix (the coil center) was obtained and the ratio of two SNR profiles measured at room and cryo-cooled temperature was calculated.

Table 2 shows five data sets of the SNR improvement ratios when using two separate coils - one matched at RT and the other one matched at LT. For each data set, the whole device was taken out of the magnet and placed into the magnet bore again before taking the images for five independent experiments. The two columns in Table 2 show an average SNR improvement of 1.50 ± 0.21 using the peak SNR comparison method (method 1) and an average SNR improvement of 1.39 ± 0.18 times when using the SNR profile method (method 2).

Table 3 shows three data sets of the Q and SNR measurements acquired (using method 2) with a single coil first matched and tuned at RT, then at LT. The Q of the coil inside the magnet bore was 28.2 ± 1.13 at room temperature and increased by a factor of 1.82 ± 0.08 after cryo-cooling to 51.4 ± 0.63. The coinciding SNR improvement calculated from images was 1.47 ± 0.11 times. The RSD was 7.5%, which is much lower than the result when using two separate coils. This is likely due to the fact that when using two coils, they are 10 mm apart resulting in some unavoidable differences, such as minor tip angle variations due to inhomogeity in the transmit field. Figure 9 shows the

SNR profile graphs as a function of y-position acquired from MR images at RT and LT (using method 2).

Table 2. SNRs before and after cryo-cooling, which were calculated by using the peak comparison method and the profile ratio method, with two separate coils − one is matched at room temperature and the other one is matched at cryo-cooled temperature.

Data Set	SNR improvement - Peak comparison - (times)	SNR Improvement - Profile ratio - (times)
1	1.81	1.50
2	1.39	1.42
3	1.62	1.63
4	1.35	1.21
5	1.34	1.21
Avg.	1.50 ± 0.21	1.39 ± 0.18

Table 3. SNR before and after cryo-cooling with a single coil matched and tuned by two varactor diodes at each temperature.

Data Set	Q factor (Room Temp.)	Q factor (Cryo-cooled Temp.)	Q Improve-ment (times)	Expected SNR Improvement (times)	Measured SNR Improvement (times)
1	29.5	51	1.73	1.56	1.46
2	27.5	52.1	1.89	1.72	1.58
3	27.6	51	1.85	1.68	1.36
Avg.	28.2 ± 1.13	51.4 ± 0.63	1.82 ± 0.08	1.65 ± 0.08	1.47 ± 0.11
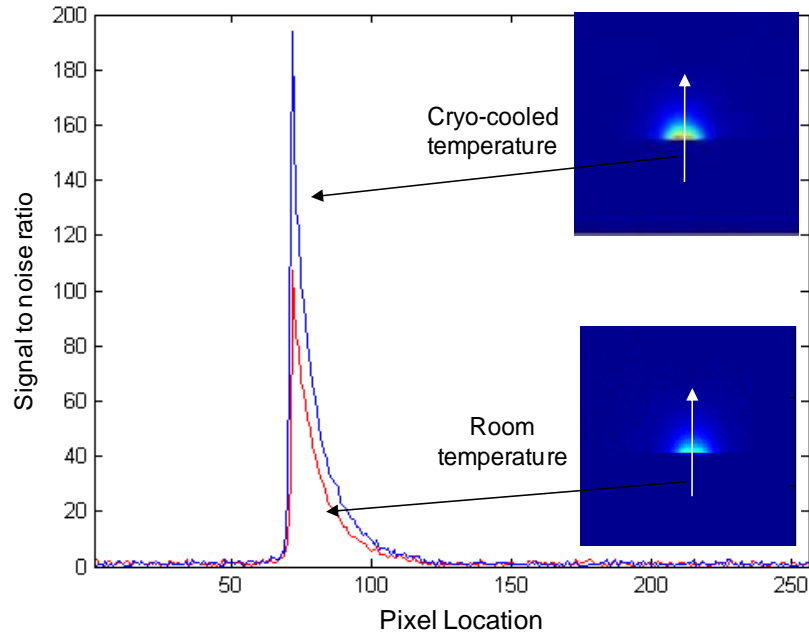
Figure 9. SNR profiles from MR images (inset) at room and cryo-cooled temperature are displayed as a function of y-position.

If all losses were due to thermal noise in the copper, cryo-cooling should yield a Q improvement of 2.83 and a corresponding SNR improvement of 3.29. Our lower Q improvement of 1.82 clearly shows the effects of the residual resistance in the matching network that was not cooled. We estimate that 70% of the resistance at RT was due to the coil, and the rest due to resistance in the matching network. Unfortunately, that 30% becomes the dominant noise source after cryo-cooling. This emphasizes the importance of low-resistance interconnects and high-Q RF components in the matching network. Further SNR improvement could be achieved by cryo-cooling the RF components. We are currently developing a revised device where the cryo-cooling microfluidic channel can also cool the tuning and matching network by directly incorporating these components on the same polymer substrate.

28

2.9. Conclusions

An integrated microfluidically cryo-cooled planar coil system for MR microscopy has been developed and SNR improved images were obtained using a 4.7T MRI system. The microfluidic channel effectively cooled the MR planar coil without any liquid nitrogen leakage or damage to the coil, and made it possible to reduce the distance between the planar coil and imaging surface without freezing the imaging surface. The effect of the liquid nitrogen microchannel on the imaging surface temperature was simulated and evaluated with the fabricated device. In addition, we selected a proper nitrogen gap thickness and nitrogen gas pressure to balance between the imaging depth and the surface temperature. The SNR improved by a factor of 1.47 ± 0.11, enabling a reduction in imaging time by a factor of two while maintaining comparable SNR to an uncooled coil. The integrated microfluidic cryo-cooling method will make it possible to obtain improved SNR from microcoils while maintaining temperatures compatible with living tissue. Importantly, the microfluidic approach can be extended to large coil arrays, potentially very important for performing wide-field-of-view MR microscopy [9]. This work has been published in Journal of Lab on a Chip [69] and the ratiometric temperature imaging part has been published in Journal of Nanoscale [23].

CHAPTER III

MULTIPLE ARRAY OF MICROFLUIDICALLY CRYO-COOLED MAGNETIC

RESONANCE (MR) PLANAR PAIR COILS

3.1. Introduction

The use of arrays of coils to replace phase encoding in MR images has been researched

to decrease scan time [7, 25-35]. Since each coil in the coil array obtains the spatial

information near the coil and the phase encoding can be replaced by the spatial

localization of each coil, the entire area of samples is reconstructed by the sum of the

collected information. As the number of coils used in arrays increases, the imaging time

decreases and the rapid imaging can be capable of capturing non-repetitive events or

turbulent flow, which is hard for conventional MRI to obtain. If SNR of the coils in the

array increase using the microfluidically cryo-cooling method without freezing samples,

the coil array can be used for smaller sample imaging or for more rapid imaging.

3.2. Design and Fabrication

The multiple array of microfluidically cryo-cooled MR planar pair coil system consists

of an array of cryo-cooling microfluidic channels through which liquid nitrogen can flow,

an array of MR planar pair coils (width: 2 mm, length: 53 mm) and an imaging surface

on which target samples to be imaged can be placed. The entire structure was the same

as the system shown in the chapter 2, except the number of cryo-cooling channels and

MR planar pair coils. The materials used for the system were PDMS and PMMA for the cryo-cooling channel material and the imaging surface structure material, respectively.

An array of coils was fabricated on a 0.5 mm thick polyetherimide (PEI) substrate. PEI has lower thermal conductivity (0.13 W/mK) than silicon (1.6 W/mK) or glass (1.1 W/mK), minimizing the heat flux between the cryo-cooled coil and the other surrounding area that is not cryo-cooled. PEI also has higher glass transition temperature (215℃) than PMMA (105℃) or polycarbonate (PC) (150℃). This makes it compatible with conventional photolithography where the use of temperatures as high as 150℃ for the photoresist hard bake step were needed for patterning MR planar coils. The MR coils were a standard planar pair design same as the SEA coil described in chapter 2, consisting of three copper traces, each being 0.25 mm wide with 0.5 mm spacing between them. The overall length of the coils was 53 mm and the distance between coils was 2 mm. To bond the planar coil substrate and the cryo-cooling microfluidic channel layer, a 0.1 mm thick spin-coated PDMS adhesion layer was used.

3.3. Optimization of Multiple Cryo-cooling Channel Dimension

The array of eight cryo-cooling channels was designed to locally cryo-cool the array of eight MR planar coils. Two types of channel distribution after the inlet area were tested (Figure 10). The first one (type 1) used one wide channel connected between the inlet and each of eight microfluidic channels and the second (type 2) used the tree-shape channel array with one channel divided into two channels with half of the width. Due the

large tree-shape area, the straight cryo-cooling channels covered 85% of the length of MR planar coils.
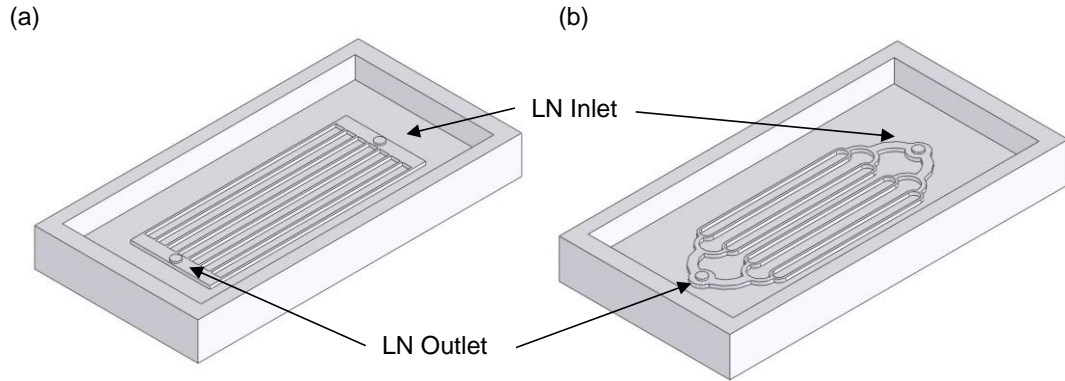
Figure 10. Master mold for fabricating eight cryo-cooling microfluidic channels: (a) Type 1 distribution channel array and (b) Type 2 distribution channel array

To investigate if liquid nitrogen evenly flows from one inlet source to each of eight microfluidic channels, temperatures of the middle and the side channel in the array were measured using a thermocouple while flowing liquid nitrogen through the cryo-cooling channel array. With the type 1 distribution scheme, the temperature difference between the middle and side channels was 30℃ (Figure 11a). With the type 2 distribution scheme, the temperature difference was 9℃ (Figure 11b), resulting in less than 10% difference in Q improvement. The type 2 distribution scheme provided stable and equal distribution of liquid nitrogen from one inlet source to each of eight microfluidic channels, thus the type 2 distribution was selected and used for the next experiments.
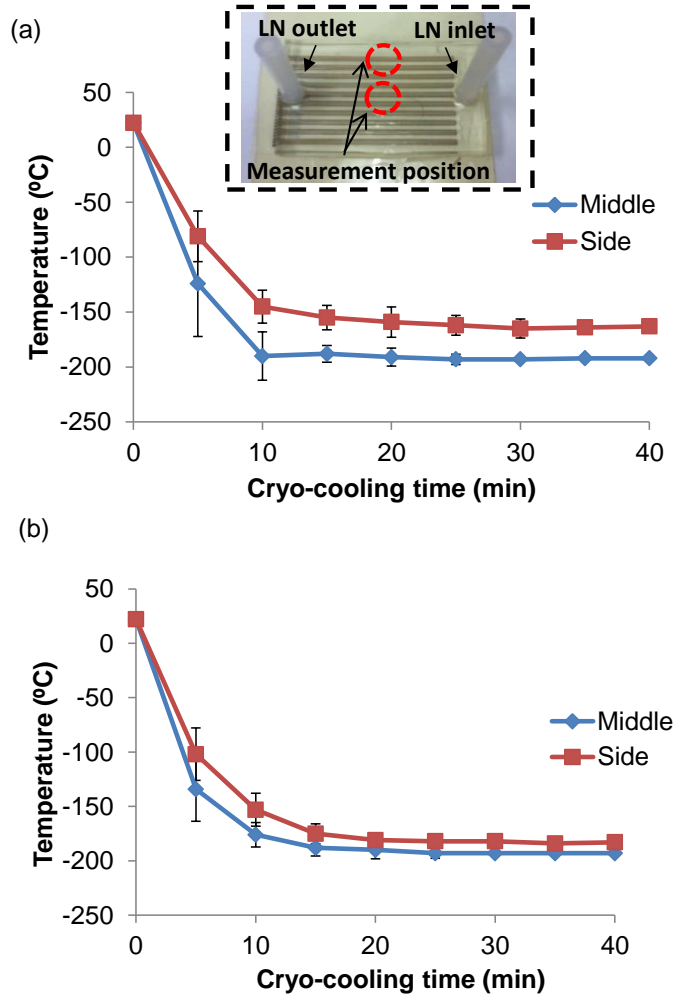
Figure 11. Temperature of the middle and side channel in the cryo-cooling channel array: (a) Type 1 distribution channel array ($n = 3$) and (b) Type 2 distribution channel array ($n = 3$)

Then, the effect of channel width on the coil temperature was simulated using commercially available FEM software (Comsol Multiphysics[TM], COMSOL Inc., Los Angeles, CA). Thermal conductivity parameters of 400 W/mK, 0.18 W/mK, and 0.13 W/mK were selected for copper, PDMS, and PEI, respectively. 27°C ambient temperature was used as the initial temperature of the structure and the surrounding. The 2 mm, 1 mm, and 0.5 mm wide straight cryo-cooling channels were selected. With 2 mm

and 1 mm wide cryo-cooling channels, the coil temperature is close the liquid nitrogen temperature. With 0.5 mm wide cryo-cooling channel, the coil temperature range was between -194℃ to -182℃ (Figure 12), resulting in Q improvement of 2.5 fold which is close to the Q improvement of 2.8 fold when cooled at liquid nitrogen temperature.
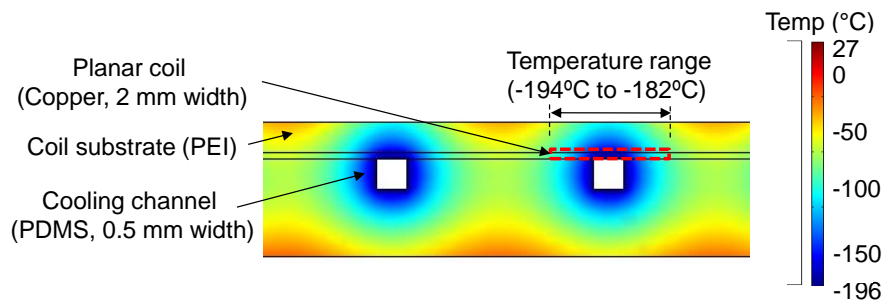
Figure 12. FEM simulation result of the device temperature profile when liquid nitrogen flows through the array of microfluidic channels. With the 0.5 mm wide cryo-cooling microfluidic channel, the temperature range of a 2 mm wide SEA coil was from -194℃ to -182℃, close to the liquid nitrogen temperature (-196℃).

Then, the temperature profile on the imaging surface was characterized with devices having three different cryo-cooling channel widths such as 0.5 mm, 1 mm, and 2 mm to verify the optimized width of straight cryo-cooling channels. The surface temperature was measured every 5 minutes for 1 hour using a thermocouple. Figure 13 shows that the array of 2 mm wide channels and the array of 1 mm wide channels did not maintain the temperature of the imaging surface above 0℃. The temperature of the imaging surface dropped below 0℃ within 10 minute cryo-cooling. With the array of the 0.5 mm wide channels, the imaging surface was kept over 0℃ for 60 minute cryo-

cooling. However, when the cryo-cooling was over 1 hr, the 0.1 % copper sulfate solution on the imaging surface started to be frozen. To solve this problem, an array of 0.3 mm wide cryo-cooling channels was fabricated and tested, but the liquid phase of nitrogen was not able to flow through the 0.3 mm wide straight cryo-cooling channels and the temperature of the coil was not dropped close to liquid nitrogen temperature, but over -50°C.
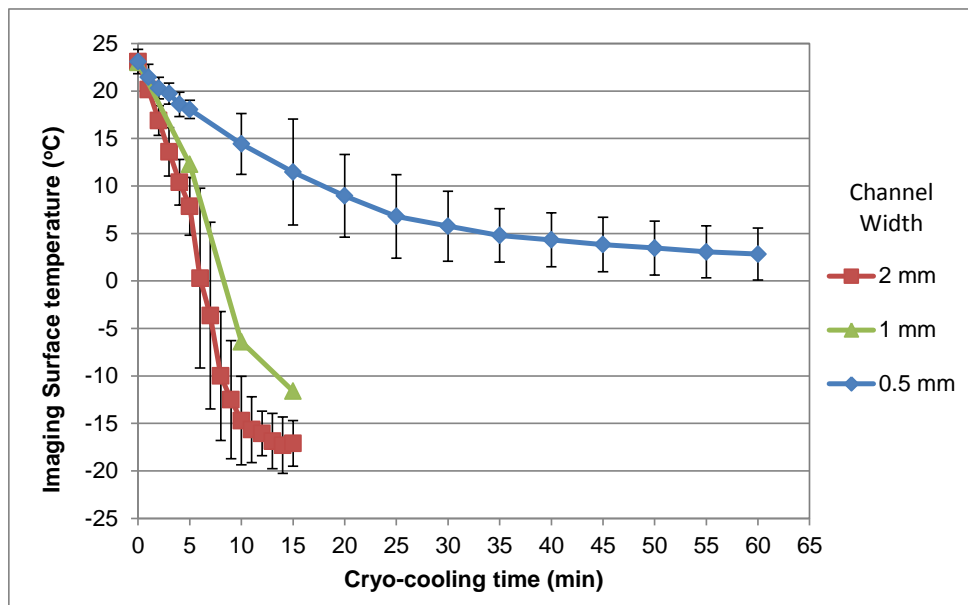
Figure 13. Imaging surface temperatures with 3 different arrays of cryo-cooling microfluidic channels having 2 mm, 1 mm, and 0.5 mm wide channels.

3.4. Q Factor Characterization

The Q factor of each MR coil was then measured with an S_{11} measurement using the network analyzer (HP4195A) after tuning the coil to 200 MHz and matching it to 50

35

ohm with 30dB return loss or better, the bandwidth Δf between the 7dB return loss

points was measured. The Q values are calculated as $Q = f_0 / \Delta f$. The coil #1 (located on

the side) and the coil #4 (located on the middle) were connected to matching/tuning

network (Figure 14) and Q factor of each coil was measured at room temperature and

cryo-cooled temperature. The array of cryo-cooling microfluidic channels is symmetric

so that the coil #1 and coil #8 (located on another side) were expected to have similar Q

improvement. With all three different channel arrays having 2 mm, 1mm and 0.5 mm

width, respectively, Q improvements of coil #1 and #4, when they were cryo-cooled,

were close to 1.8. The coil #4 tended to show higher Q improvement than the coil #1.

The cryo-cooling microfluidic channels was designed to provide even distribution of

liquid nitrogen, but small difference of fluidic resistance of each cryo-cooling channel

made during the fabrication steps generated different liquid nitrogen flow between the

channels #3 to #6 (placed near the middle of the cryo-cooling channel array) and the

fluidic channel #1, #2, #7, and #8 (placed closed to side of the cryo-cooling channel

array). However, both coils #1 and #4 have Q improvement of over 1.7 fold and are

expected to have about 1.45 times SNR improvement based on the result of chapter 2.

	Q improvement		
	2 mm width	1mm width	0.5 mm width
Coil #1	1.74	1.69	1.72
Coil #4	1.88	1.84	1.81
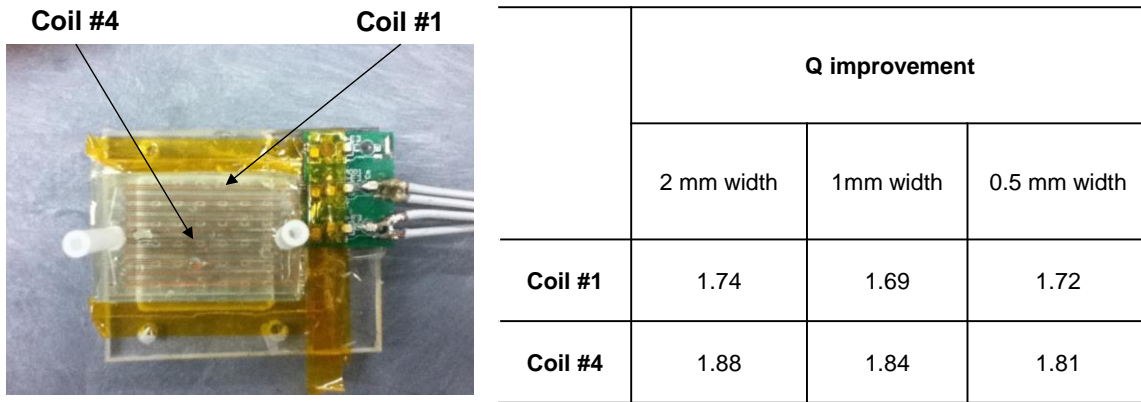
Figure 14. The assembled multiple microfluidically cryo-cooled MR planar pair coils device. Two coils (placed at side and middle) were tested for Q characterization. The Q enhancement was close to 1.8 fold which is similar to the Q enhancement obtained in chapter 2.

3.5. Conclusions

The developed single cryo-cooling channel in chapter 2 has been applied to an array of MR planar pair coils to conduct "Single-Echo Acquisition (SEA)" imaging with multiple SEA coils for small sample imaging. The array of eight cryo-cooling channels was designed to have liquid nitrogen flow evenly through eight cryo-cooling channel placed above the array of eight MR planar pair coils. A significant improvement in Q factor was demonstrated similar to the Q improvement (1.8 fold) obtained in chapter. Within 1 hr cryo-cooling, the temperature on the imaging surface was able to maintain above 0°C and it may enable multiple cryo-cooled planar pair coils to conduct fast imaging with improved SNR.

CHAPTER IV

MICROFLUIDICALLY CRYO-COOLED MR PLANAR MICROCOIL WITH

INDUCTIVELY COUPLING

4.1. Introduction

Magnetic resonance (MR) microscopy has been enabled largely by the enhanced

sensitivity obtained when using a microcoil, a small diameter coil that matches the

sample size in scale, inducing a higher RF magnetic field strength per unit current [36,

37]. Various miniaturized transceiver or receiver coils such as solenoidal microcoils and

planar microcoils have been developed in the past decade [37-49].

As coils get smaller, thermal noise from the conductors becomes the primary

source of loss, reducing SNR as compared to what could be achieved if the sample were

the dominant noise source. Conventional thought would suggest cryo-cooling of copper

coils or the use of high temperature superconducting (HTS) coils to minimize the

Johnson (thermal) noise of the coils and to improve SNR [4, 5, 50-56]. In fact, cryogenic

cooling techniques have been used in a few small (centimeter-wide) coils using

inductive coupling [3, 56-58]. Due to the bulkiness of conventional cryostats, however,

the coil to sample distance is typically not suitable for cryo-cooling microcoils since the

most sensitive region of a coil is within approximately its diameter, requiring a very

small sample to coil distance.

A microfluidically cryo-cooled MR coil system using planar pair coils was

developed as described in chapter 2 and preliminary data for a microfluidically cryo-

cooled spiral microcoil were presented [59-61]. The system successfully cryo-cooled the coil locally to liquid nitrogen temperature (-196℃) using a cryo-cooling microfluidic channel enclosing the coil, and demonstrated quality factor (Q) enhancement of 1.8 times and SNR enhancement of 1.5 times without freezing samples placed less than 2 mm away from the coil. However, these values were lower than the theoretically predicted Q factor enhancement of 2.8 times and SNR enhancement of 3.3 times [4]. Further investigation revealed that the resistance of the tuning and matching network was higher than that of the microcoil itself, and thought to be the probable cause of the lower-than-expected Q and SNR enhancements. However, cryo-cooling the matching/tuning network was not possible using the microfluidic method due to both the bulkiness of conventional off-chip capacitors used for matching/tuning (several millimeter in widths and height) as well as the direct transmission line connection to the MR system that prevents a microfluidic channel from enclosing all these components for cryo-cooling.

To overcome these challenges, a microfluidically cryo-cooled planar microcoil with an integrated microfabricated parallel plate capacitor was developed and is presented here. The planar and integrated nature of the microfabricated capacitor allowed both the microcoil and the capacitor to be embedded inside a cryo-cooling microfluidic channel, while maintaining all the advantages of microfluidically cryo-cooling, namely the small coil-to-sample distance and minimized temperature effect on the imaging surface from the liquid nitrogen flowing through the cryo-cooling microfluidic channel. Physical transmission line connections to the microcoil were

39

eliminated by using inductive coupling in order to allow cryo-cooling of the integrated resonating capacitor, in which signals detected by the primary microcoil in close proximity to the sample are coupled inductively to a secondary coil, which is then directly connected to the MR system through a transmission line. This method also increased cooling efficiency, since it prevented heat leakage through the transmission line. In addition to enabling the microcoil and the resonating capacitor to be cooled efficiently, a second minor but possibly important advantage of the inductive coupling arrangement is that it lets the microcoil be repositioned more easily than would be the case if the transmission line were connected to it directly. This may be advantageous due to the small field-of-view of the microcoil [62].

While inductive coupling does degrade the SNR somewhat due to additional losses caused by the secondary coil [63], it has been shown that such degradation can be kept to a minimum [64]. In fact, despite the small drop in SNR, inductive coupling has been used for several applications in MRI, such as enabling easily reconfigurable coil arrays [65], implantable probes for organ imaging [66], widening the bandwidth of the coil [67], and parallel MR imaging [68]. Recently, inductive coupling has also been used successfully in conjunction with microcoils. Sakellariou *et al.* used an inductively coupled solenoidal microcoil around a capillary tube to conduct a magic angle spinning experiment [69] and Utz *et al.* presented a solenoidal microcoil inside a commercial NMR probe to monitor flow inside a capillary [70]. Ryan *et al.* presented planar microcoils on a microfluidic chip inductively coupled to an NMR probe [44]. However inductive coupling of planar microfabricated coils for MRI applications have not been

40

utilized in microfluidically cryo-cooled coil applications to maximize the cooling efficiency.

This chapter describes an inductively coupled microfluidically cryo-cooled spiral microcoil with an integrated microfabricated parallel plate capacitor which is able to be fabricated in the formation of an array of coils for potential applications in MR microscopy or lab-on-a-chip systems.

4.2. Theory

4.2.1. Effects of Cooling

When thermal noise from the conductors is the dominant noise source in coils, the SNR is proportional to the inverse of the square root of temperature and resistance as can be seen in (3) [71]:

$$SNR = \frac{V_{signal}}{V_{noise}} = \frac{V_{signal}}{\sqrt{4k_bTR\Delta f}} \propto \frac{1}{\sqrt{TR}} = \sqrt{\frac{Q}{T \cdot 2\pi f L}} \tag{3}$$

where k_b is the Boltzmann's constant, T is the temperature, R is the electrical resistance of the coil, f is the frequency, L is inductance of the coil and Q is the quality factor. In a series resonant circuit, $Q = 2\pi fL/R$. Reduced R results in smaller thermal noise, leading to a higher Q.

L does not change when the coil is cooled and the frequency is unchanged, therefore, the expected SNR improvement by cooling the coil can be given by:

41

$$SNR_{improvement} = \frac{SNR_{cooled}}{SNR_{room}} = \sqrt{\frac{T_{room}/Q_{room}}{T_{cooled}/Q_{cooled}}} \qquad (4)$$

When copper is cooled from room temperature to liquid nitrogen temperature (77K), its resistivity decreases by a factor of eight [18]. However, because the skin depth is proportional to the square root of resistivity, the high frequency resistance of copper at room temperature decreases by a factor of $\sqrt{8}$ (= 2.83) at liquid nitrogen temperature. Thus, the ideal SNR improvement obtained by cryo-cooling a copper coil to liquid nitrogen temperature is 3.3 fold [4].

4.2.2. Inductive Coupling

Figure 15 illustrates the concept of inductively coupled coils. The mutual inductance, an indicator of the degree of coupling efficiency, can be written as $M = k\sqrt{L_p L_s}$ [70], where k is the coupling constant and L_p and L_s are the inductance of the primary coil (microcoil) and the secondary coil, respectively.
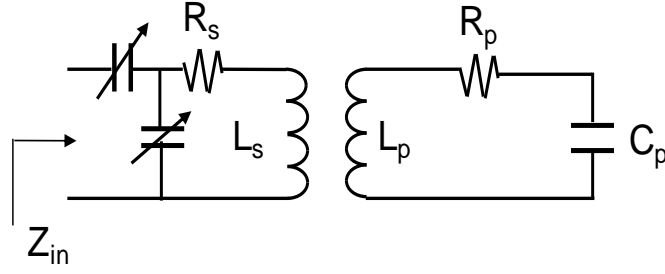
Figure 15. Conceptual circuit diagram for inductively coupled primary microcoil and secondary coil. L_p and L_s are the inductance of the microcoil and the secondary coil, respectively. R_p and R_s are the resistance of the microcoil and the secondary coil, respectively. C_p is the capacitor to resonate the microcoil at 200 MHz.

Measuring the variation in input resistance of the secondary coil is a standard and straightforward indicator of the mutual inductance or coupling efficiency, since the level of coupling changes with coil geometry and relative placement of the two coils. For a coupled system at room temperature, the ratio of the SNR of the coupled coil system to the SNR of the primary coil alone can be estimated by [64]:

$$\delta = \frac{SNR_c}{SNR_p} = \sqrt{\frac{R_{in} - R_s}{R_{in}}} \tag{5}$$

R_{in} and R_s are the input resistance of the secondary coil coupled to the primary coil and the resistance of the secondary coil alone, respectively. To prevent a decrease in SNR of more than ten percent, we can show that R_{in} should exceed that of the secondary coil alone by a factor of approximately five:

43

$$R_{in} \geq \frac{R_s}{1-\delta^2} \approx 5.26 R_s \tag{6}$$

Since ideal direct coupling (transmission line connection) would create severe heat losses, sustaining a decrease in SNR of 10% or less due to inductive coupling was a reasonable sacrifice. In the case where the secondary coil is at room temperature, the resistive noise contributed by the secondary coil is at a higher noise temperature, and Eq. 5 can be modified to:

$$\delta = \frac{SNR_c}{SNR_p} = \sqrt{\frac{R_{in} - R_s}{R_{in} + R_s \left(\dfrac{T_s}{T_p} - 1 \right)}} \tag{7}$$

where T_s is the temperature of the secondary coil and T_p is the temperature of the primary coil. For a room temperature system, Eq. 7 reduces to Eq. 5, as expected. In this case, Eq.6 can be modified to:

$$R_{in} \geq \frac{R_s}{1-\delta^2} \left(1 + \delta^2 \left(\frac{T_s}{T_p} - 1 \right) \right) \tag{8}$$

Again, for a room temperature coil, Eq. 8 reduces to Eq. 6, as expected. In this case, to ensure the factor of less than ten percent degradation in SNR by using inductive

coupling rather than physical connections, we can see that $R_{in} \geq 17R_s$ when the primary

coil is cooled to 77°K and the secondary coil is at room temperature. The decrease in

resistance of the cooled primary coil will account for nearly a factor of 17 increase in

input resistance through the equations for the coupled circuit. Ultimately this places a

lower bound on the size of the coil that can be used with a particular secondary coil

without incurring an unacceptable loss in SNR due to inductive coupling.

4.3. Design and Fabrication

The cryo-cooled and inductively coupled microcoil device is composed of four layers as

shown in Figure 16; a spiral surface microcoil for MR imaging (primary coil), a cryo-

cooling microfluidic channel through which liquid nitrogen (LN) flows, a secondary coil

for inductive coupling, and an imaging surface structure. The dimensions of the primary

microcoil were chosen to be similar to that of Massin et al., who reported a planar spiral

microcoil with high sensitivity [37]. A planar microcoil (2 mm inner diameter (ID), 3

turns, 40 μm trace width, 30 μm spacing, and 25 μm thick) was fabricated on a 0.5 mm

polyetherimide (PEI) sheet. PEI has lower thermal conductivity (0.13 W/mK) than

silicon (1.6 W/mK) or glass (1.1 W/mK), minimizing the heat flux between the cryo-

cooled coil and the other surrounding area that is not cryo-cooled. PEI also has higher

glass transition temperature (215°C) than poly(methyl methacrylate) (PMMA) (105°C)

or polycarbonate (PC) (150°C). This makes it compatible with conventional

photolithography where the use of temperatures as high as 150°C for the photoresist hard

bake step were needed for the integrated parallel plate capacitor microfabrication. To

resonate the microcoil at 200 MHz, the Larmor frequency of the 4.7 Tesla (T) MRI system used for imaging, a parallel plate capacitor (6.3 mm^2 area) with a 15 µm thick SU-8 dielectric layer was microfabricated. A 3 mm wide and 1 mm high microfluidic channel was fabricated using poly(dimethylsiloxane) (PDMS) and bonded underneath the "microcoil-capacitor resonator" (microfabricated microcoil + microfabricated parallel plate capacitor), allowing for cryo-cooling of the entire microcoil resonator structure.
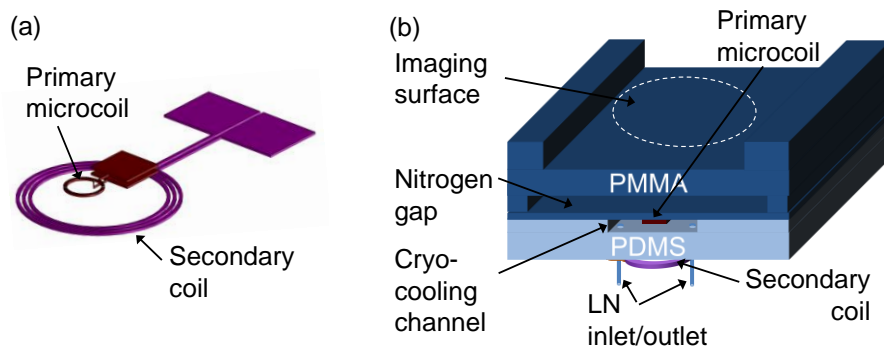
Figure 16. Schematic of the microfluidically cryo-cooled and inductively coupled MR microcoil device. (a) Primary spiral microcoil (2 mm inner diameter (ID), 3 turns, 40 µm trace width, 30 µm spacing, and 25 µm thickness) with an on-chip capacitor and the secondary coil (1 cm ID, 3 turns using 18 gauge magnet wire). (b) Cross sectional view of the integrated device. The nitrogen gas gap is 1.0 mm wide and the microcoil substrate is 0.5 mm thick. The total distance between the microcoil and the imaging sample is 1.8 mm. The distance between the primary microcoil and the secondary coil is 5 mm

The secondary coil (1 cm ID, 3 turn solenoid) for inductive coupling was hand-wound from 18 gauge wire and positioned under the primary microcoil bonded with the cryo-cooling channel. To fix the position of the secondary coil, the coil was sealed with

46

additional PDMS after alignment. The matching network of the secondary coil was designed and constructed with conventional capacitors and connected with standard RG-58 50 Ω coaxial cable to the MR system.

The imaging surface on which samples are placed was separated from the microcoil substrate using a 1 mm high nitrogen gas gap supported by two vertical side-support structures. This provided thermal isolation during cryo-cooling of the microcoil system to prevent samples from freezing during MR image acquisition, while minimizing the coil-to-sample distance. The final distance between the coil and sample was 1.8 mm, less than the several millimeters of coil-to-sample distance previously reported by other researchers [53, 72, 73]. It is worth noting that Bruker's Cryoprobe™ provides 1 mm separation between the coil and sample, but does require an additional heating device to keep the sample from freezing [74].

Figure 17 illustrates the overall fabrication steps of the MR surface microcoil and the integrated parallel plate capacitor. A chromium/copper (30/300 nm) seed layer was deposited on a 0.5 mm thick and 76 mm x 76 mm PEI substrate (Ultem® 1000, SabicGE Plastics, Boedeker Plastics, Shiner, TX) using an electron-beam evaporator (Figure 17a). Then, a 35 µm thick photoresist (NR21-20000P, Futurrex Inc., Franklin, NJ) was spun, and the microcoil and the bottom side plate of the parallel plate capacitor were defined using a photolithography process (Figure 17b). Following photolithography, 25 µm of copper was electroplated using a copper sulfate solution ($CuSO_4 : H_2SO_4 : H_2O = 250$ g : 25 ml : 1 L) at a current density of 10 mA/cm^2. The photoresist was removed by photoresist remover (RR4, Futurrex Inc.) instead of commonly used acetone to prevent

the PEI substrate from being damaged by the solvent. The chromium/copper seed layer

was etched by chrome etchant (TFE, Transene Company Inc., Danvers, MA) and copper

etchant (CE-100, Transene Company Inc) (Figure 17c).
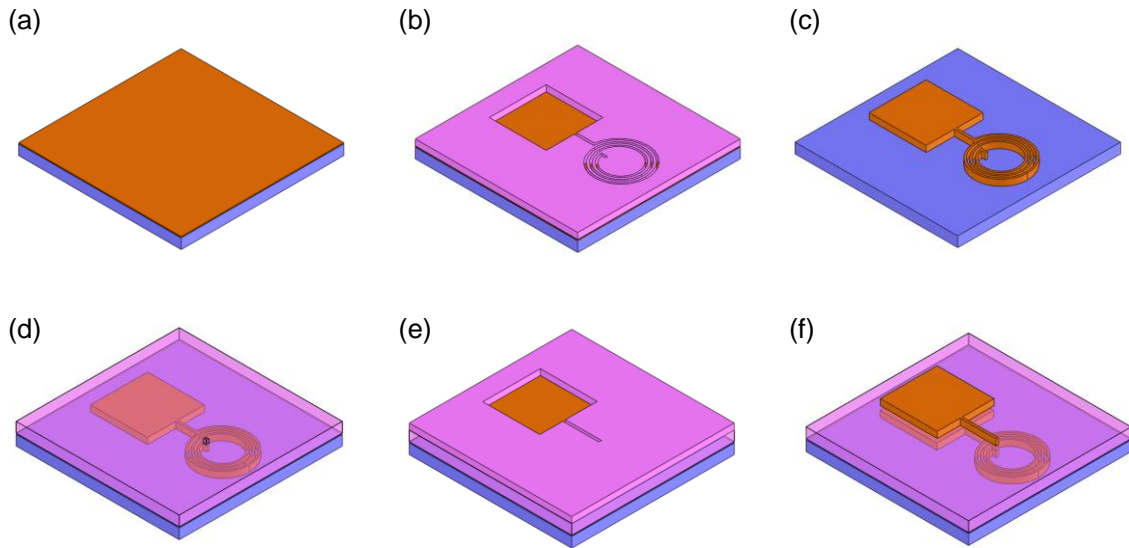
Figure 17. Fabrication processes for the spiral microcoil and the integrated parallel plate capacitor. (a) Cr/Cu seed layer deposition on a thin substrate. (b) negative photoresist patterned to define the lower capacitor plate and the microcoils. (c) Cu electroplating to 25 µm height, removal of the photoresist and the Cr/Cu seed layer. (d) SU-8™ patterned for the dielectric layer of the capacitor and the connection post between the coil and the capacitor, followed by Cu electroplating. (e) Cr/Cu seed layer deposition on the SU-8™ layer and negative photoresist patterning to define the upper capacitor plate and the connection traces between the coil and the capacitor. (f) Cu electroplating to 25 µm height, removal of the photoresist and the Cr/Cu seed layer.

.

Afterwards, the coil substrate was coated with a 15 µm thick SU-8™ 2015 layer

(MicroChem, Newton, MA) as the dielectric layer between the parallel plate capacitor.

A post for electrical connection between the microcoil and the capacitor was defined

using a second photolithography step, followed by electroplating copper to a thickness of

15 µm (Figure 17d). The relative permittivity of SU-8™ is 4.1 at 1 GHz at room temperature [75]. The substrate was then placed on a 150°C hot plate for 30 min to hard-bake the SU-8 layer. Then, another chromium/copper (30/300 nm) seed layer was deposited on the substrate and a 35 µm thick NR21-20000P photoresist layer was coated on it to photolithographically define the top side plate of the parallel plate capacitor (Figure 17e). After electroplating of a 25 µm thick copper layer using the photolithographically defined electroplating mold of the top capacitor plate, the metal seed layer and the photoresist were removed (Figure 17f). Finally, a 30 µm thick PDMS layer was coated on the substrate to bond the microcoil resonator system to the cryo-cooling microfluidic channel. This also prevented the microcoil resonator system from being detached from the substrate due to thermal stress during cryo-cooling.

The cryo-cooling microfluidic channel for liquid nitrogen delivery to the microcoil was fabricated in PDMS using soft lithography (Figure 18). The acrylic master mold was cut using a rapid prototyping machine (MDX-40, Roland DGA Corp., Irvine, CA). After 3.18 mm outer diameter (OD) silicone tubings were placed on the inlet and outlet area of the master mold, uncured PDMS was applied to the mold. The released polymerized PDMS replica from the master mold was then bonded to the previously fabricated microcoil substrate coated with a thin PDMS layer.
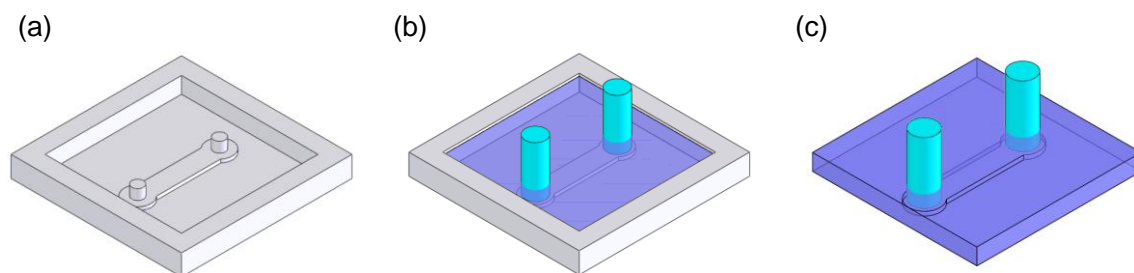
Figure 18. Fabrication steps for the cryo-cooling microfluidic channel structure. (a) Acrylic master mold fabrication using a rapid prototyping machine. (b) Silicone tubing insertion and PDMS pouring. (c) PDMS curing and releasing

The secondary coil was positioned 5 mm below the primary microcoils (Figure 19a, b). To fix the position of the secondary coils, the coils were sealed with additional PDMS after the alignment. The nitrogen gap and the imaging surface were created in an acrylic block ($80 \times 210 \times 12$ mm^3) using the rapid prototyping machine. A small pillar array (1 mm in width, 2 mm in length, and same height as the nitrogen gap) was fabricated inside the nitrogen gap to prevent the gap from collapsing under an external clamping force required for the final assembly.

For the final assembly step, the planar coil substrate bonded with the cryo-cooling microfluidic channel was attached to the acrylic frame using Kapton tape to form the closed nitrogen gap channel (Figure 19c). Nylon screws were used to clamp this sandwich structure to an acrylic cradle, which was loaded to the center of the magnet. The liquid nitrogen tubing and nitrogen gas tubing (6.35 mm OD polyethylene tubing) were attached to the acrylic board, and the liquid nitrogen dewar (Lab20 with withdrawal, Chart Industries, Inc., Garfield Heights, OH) and the nitrogen gas cylinder were connected to the liquid nitrogen tubing and nitrogen gas tubing, respectively. To

drive liquid nitrogen out from the dewar, nitrogen gas was pumped into the dewar. To

prevent heat loss due to conduction and convection in the polyethylene tubing used for

liquid nitrogen delivery to the PDMS microfluidic channel, the tubing was wrapped with

insulating sponge foam tape (Frost King, Mahwah, NJ).
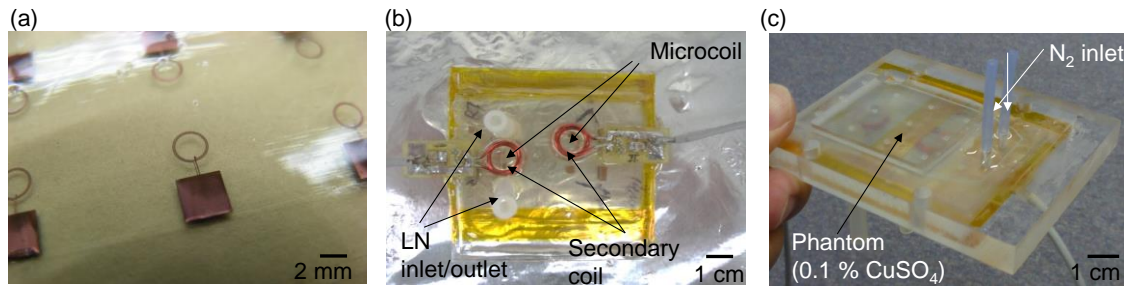
Figure 19. (a) Microfabricated spiral microcoils with an integrated parallel plate capacitor for resonating at 200 MHz at RT and LT. (b) Integrated device with the microcoil resonator, a LN cryo-cooling channel, and a secondary coil. The image shows two systems on a single substrate. (c) The device having an imaging phantom (0.1% $CuSO_4$) on top of the imaging surface ready for MR imaging.

4.4. Characterization of Inductive Coupling Efficiency

Before characterizing the Q factor of the fabricated microcoil resonator system, the

coupling efficiency between the primary microcoil resonator and the secondary coil was

first characterized. Input resistance of the secondary coil (open-circuited) was measured

using a network analyzer (HP 4195A) and used as the indicator of the ratio of the SNR

of the coupled coil system to the SNR of the primary coil alone as explained in the

theoretical discussion of inductive coupling above.

The measurement of an input resistance less than 1 ohm using a conventional network analyzer is extremely difficult because the accuracy of a network analyzer is over 1 ohm error in input resistance for a 50 ohm system [76]. Hence, the Q of the secondary coil at 200 MHz was measured instead of the resistance, and the resistance of the secondary coil was then calculated using the R-L-C circuit equation of $R = \omega L / Q$, where ω is the angular frequency and L is the inductance. Using this method, the input resistance of the isolated secondary coil at 200 MHz was calculated to be 0.69 ohm.

When the secondary coil was centered 5 mm above the cryo-cooled microcoil-capacitor resonator, an input resistance of 7.22 ohms was measured. Since this resistance was about 9.6 times larger than the input resistance measured without inductive coupling, this inductive coupling resulted in approximately 17% degradation in SNR. As described in the theoretical discussion of inductive coupling above (Section 4.2.2), the input resistance should increase 17 times to maintain less than 10 percent degradation in SNR. Therefore, in future work, to obtain higher coupling efficiency, the number of turns on the microcoil needs to be increased or the coil (microcoil and secondary coil) dimensions and geometry should be optimized. However, for the purpose of demonstrating the effectiveness of microfluidically cryo-cooling the resonating capacitor as well as the microcoil, it was not necessary to optimize the inductive coupling.

4.5. Characterization of the Microfabricated Capacitor

The characteristics of the microfabricated capacitor at room temperature (RT) and liquid nitrogen temperature (LT) were important parameters to be considered when characterizing the Q and SNR improvement due to cryo-cooling. Therefore, to examine changes in the relative permittivity of the SU-8 layer at RT and LT (which would affect resonant frequencies) and the dielectric loss at RT and LT (which would affect relative Q improvement), an isolated parallel plate capacitor (3 mm × 4 mm) with a 15 µm thick SU-8™ dielectric layer was fabricated without an accompanying microcoil. The network analyzer was calibrated with a coaxial probe using port extension and compensation. This probe was then soldered to the microfabricated capacitor. The capacitance and series resistance of the capacitor were measured at RT and then LT after immersing the capacitor in a liquid nitrogen bath in order to characterize the effects of the microfabricated capacitor alone.

At RT, the microfabricated capacitor had a capacitance of 31 pF. At LT, the capacitance decreased to 24 pF. Based on the measurement, the relative permittivity of SU-8 at 200 MHz can be estimated to be 4.3 at RT and 3.4 at LT. The 22% decrease in capacitance measured after cryo-cooling resulted in a shift of the resonant frequency of the microcoil resonator and corresponded well to an observed 12% increase in resonant frequency during cryo-cooling according to the LC resonance equation ($\omega = 1/\sqrt{LC}$). The practical effect of the change of the relative permittivity of SU-8 is that two separate microcoils were required to be fabricated in order to tune the coils at RT and LT, respectively.

53

Unfortunately, along with the dielectric constant, the dielectric loss in the SU-8 also changed with temperature (higher at room temperature), making the Q improvement (Q at LT (Q_{LT}) vs. Q at RT (Q_{RT})) for the microcoil-capacitor resonator artificially high (Q improvement of 5.8 times). The dielectric loss of the microfabricated capacitor was characterized by measuring its series resistance. At RT, the microfabricated capacitor had a series resistance of 1.5 ohms and at LT, the series resistance became too small to measure. The high series resistance of the SU-8 layer at room temperature (=1.5 ohms) resulted in a low Q_{RT} of the microcoil resonator, artificially increasing the ratio of Q_{LT} to Q_{RT}. Therefore, the comparison was made to the Q of a conventional microcoil at RT (described in the next section (Section 4.6)), instead of the microcoil-capacitor resonator at RT.

4.6. Q Improvement

To characterize the expected improvement in SNR that could be achieved by the microcoil-capacitor resonator compared to a "conventional microcoil", the Q of the microcoil-capacitor resonator at RT and LT was measured on the bench and compared to the Q of a conventionally tuned and fed microcoil. Specifically, the same spiral microcoil was used at RT and LT, but tuned with high-Q varactors (MV34009, Microsemi, Lowell, MA) rather than the microfabricated capacitor and connected with a transmission line rather than inductively coupled. The microcoil-capacitor resonator was tuned to the operating frequency of 200 MHz by trimming small areas of the capacitor under a microscope until the desired resonant frequency was reached.

The Q of the microcoil-capacitor resonator was measured as $Q = f_0/\Delta f$, where f_0 is the center frequency of the resonator and Δf is the half power bandwidth, from the S_{21} measurement after two decoupled probes were brought close to the microcoil-capacitor resonator. For the Q measurement of the conventional microcoil, the transmission line of the conventional microcoil was connected to the HP 4195A network analyzer, and f_0 and Δf_{7dB} (bandwidth of the -7dB points on the S_{11} measurement) were measured. The measurement with this technique has been shown previously to agree with the dual probe method for unloaded Q measurement [24, 77].
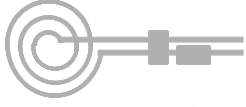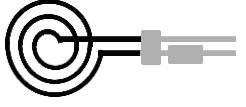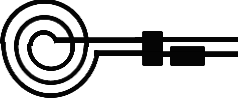
To cryo-cool the "conventional microcoil", the coil plus matching/tuning network was physically dipped in liquid nitrogen. Since such setup is not feasible for imaging, these comparison measurements were restricted to the bench measurement of Q factors. The Q factor improvement of the microcoil-capacitor resonator was characterized by comparing the Q factor of the microcoil-capacitor resonator at LT to the Q factor of the conventional microcoil at RT. This Q factor improvement was then compared to the Q factor improvement of the conventional microcoil at LT against RT. The expected improvement in SNR using the microcoil-capacitor resonator against the conventional microcoil was estimated by:

$$\text{SNR}_{improvement} = \sqrt{\frac{293K}{77K} \cdot Q_{improvement}} \tag{9}$$

as described theoretically by Eq. 4.

55

Table 4 summarizes the Q measurements acquired at RT and LT from two microcoils, one using high-Q varactors with a transmission line (conventional microcoil) and another one using the microfabricated on-chip capacitor without a transmission line (microcoil-capacitor resonator). With the microcoil using high-Q varactors, the Q increased by 1.8 fold when microfluidically cryo-cooling only the microcoil. The Q further increased by 2.4 fold when both the microcoil and the matching/tuning network were cryo-cooled through direct dipping in liquid nitrogen. The Q improvement when comparing the conventional microcoil at RT, $Q_{RT,Var}$ (= 26.7), to the microcoil-capacitor resonator at LT, $Q_{LT,ChipCap}$ (= 70), was 2.6 fold. This improvement matches well to the theoretically predicted Q enhancement of 2.8 fold when cryocooling both the coils and the matching/tuning network [61], and is significantly higher (= 144%) than the Q enhancement of 1.8-fold previously achieved by our team when cryo-cooling only the microcoil and not the matching/tuning network. In addition, as validation, this Q improvement of 2.6 times obtained from the microcoil-capacitor resonator was in line with the Q improvement of 2.4 (= 63.7/26.7) obtained when comparing the Q of the conventional microcoil at RT ($Q_{RT,Var}$ = 26.7) to LT ($Q_{LT,Var}$ = 63.7) obtained when directly dipping the conventional microcoil and varactors into a liquid nitrogen bath. Therefore, the developed microfluidically cryo-cooled microcoil resonator system performance is in line with a microcoil system with off-chip varactors, at the same time providing much better integrability, system compactness, practicality, and ease of system production.

56

Table 4. Q factor of a directly coupled 3-turn microfabricated spiral microcoil at room temperature and liquid nitrogen temperature. (Gray indicates room temperature components and black indicates cryo-cooled components.)

	Q_{RT}	Q_{LT} (Cryo-cooling only microcoil)	$Q_{LT,both}$ (Cryo-cooling both microcoil and matching/tuning network)
Microfabricated coil resonated with high-Q varactors	varactor $Q_{RT,Var} = 26.7$	varactor $Q_{LT,Var} = 47.1$ $(Q_{LT,Var}/Q_{RT,Var} = 1.8)$	varactor $Q_{LT,both,Var} = 63.7$ $(Q_{LT,both,Var}/Q_{RT,Var} = 2.4)$
Microfabricated coil resonated with on-chip capacitor	on-chip capacitor $Q_{RT,ChipCap} = 12$ (Note: Q of micro-fabricated capacitor is very low due to lossy SU-8)		on-chip capacitor $Q_{LT,ChipCap} = 70$ $(Q_{LT,ChipCap}/Q_{RT,Var} = 2.6)$

4.7. MR Imaging

Imaging was performed in a 4.7T MRI system (40 cm bore, Unity/Inova console, Varian, Palo Alto, CA). RT MR images of a phantom (0.1% copper sulfate solution) were acquired in the axial plane (perpendicular to the imaging surface and the plane of the coil), with the coil operating in transmit/receive mode in order to avoid the additional complexity of decoupling from a separate transmit coil. All images were acquired using a standard spin echo sequence with a matrix size of 128×128, field-of-view of 50×30 mm, TR (repetition time) of 500 ms, TE (echo time) of 31 ms, two averages, slice thickness of 0.5 mm, and spectral width of 20 kHz. Once 10 and 16 dB for 90°/180° tipping was selected, RT images were acquired in the axial plane. LT images were then obtained after flowing liquid nitrogen to the microcoil.

MATLAB® was used to reconstruct images and evaluate image SNR. An SNR matrix was obtained by dividing the signal magnitude matrix by the average value of a large noise region outside the phantom.

Figure 20a shows the position of the primary microcoil and the secondary coil, the nitrogen gap, and the phantom to be imaged. Figure 20b shows the image obtained by the secondary coil without the microcoil-capacitor resonator coupled. It shows a much larger area excited by the secondary coil than when the microcoil-capacitor resonator coupled (Figure 20c). This shows that the sensitivity pattern of the inductively coupled system is dominated by the primary coil, as suggested by the resistance measurements with the microcoil coupled to the secondary coil. Figure 20c and d show the transverse images obtained at RT and LT with the microcoil coupled to the

secondary coil. SNR comparison of both images was not considered valid due to the

artificial Q improvement between RT and LT discussed in Section 4.6.
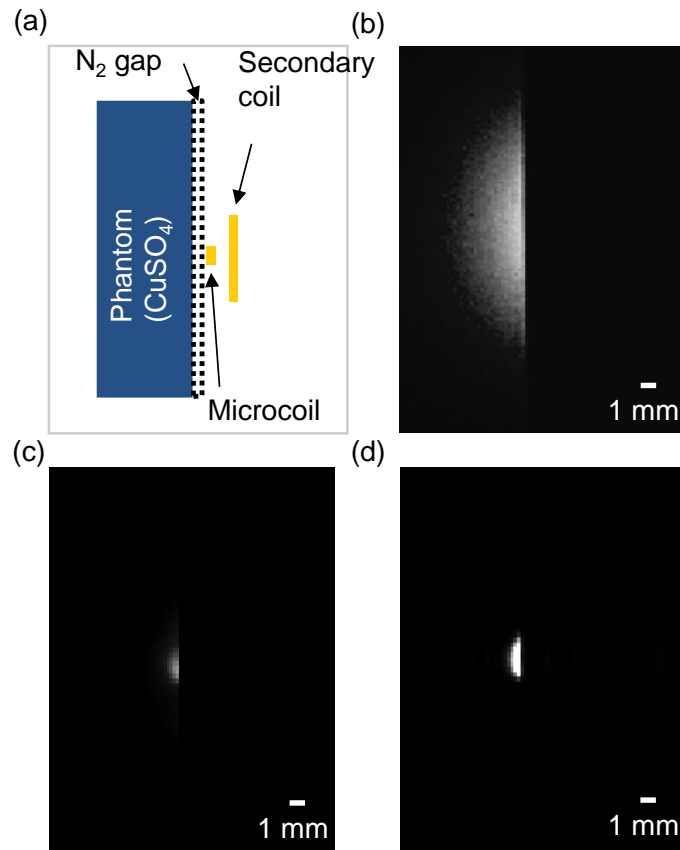
Figure 20. Transverse spin echo images, acquired with the secondary coil, RT microcoil and LT microcoil (using 50 x 30 mm field of view and approximately 90° 180° flip angles). (a) Illustration of the position of the phantom, the microcoil, and the secondary coil. (b) Secondary coil image (no microcoil coupled). (c) RT microcoil image. (d) LT microcoil image.

4.8. Analysis the Effects of Coil-to-Sample Distance

In this design, the nitrogen gap of 1 mm, the microcoil substrate of 0.5 mm, and the imaging surface of 0.3 mm together lead to a coil-to-sample spacing of 1.8 mm. As the focus of this particular work was to increase the improvement in Q achieved with microfluidic cryo-cooling to match the theoretically predicted Q improvement, minimizing the coil-to-sample distance was not of immediate concern. However, for completeness, the system was modeled to predict the coil-to-sample spacing at which cryo-cooling no longer provides a benefit over a conventional, uncooled coil placed directly on the sample. The microcoil dimensions used in the simulation were the same as the cooled coil described above (inner diameter: 2 mm, trace width: 40 µm, trace gap: 30 µm, and the height of trace: 25 µm). The feed loop trace was 100 µm below the main trace and the capacitor used to resonate the microcoil at 200 MHz was assumed to be lossless. A coil-to-sample spacing of 0.2 mm was used, which was the minimum distance in practice due to the thickness of the imaging surface substrate.

Figure 21 shows the simulated relationship between the normalized relative SNRs of a cryo-cooled microcoil and an uncooled microcoil against coil-to-sample distance. The normalized relative SNR of the uncooled microcoil with 0.2 mm of coil-to-sample distance is about 0.95. To match this or provide improvement, the cryo-cooled microcoil needs to have a coil-to-sample distance of 1.25 mm or less. If 10% degradation in SNR, which is a reasonable sacrifice due to inductive coupling, is taken into account, the distance has to be 1.15 mm or less.
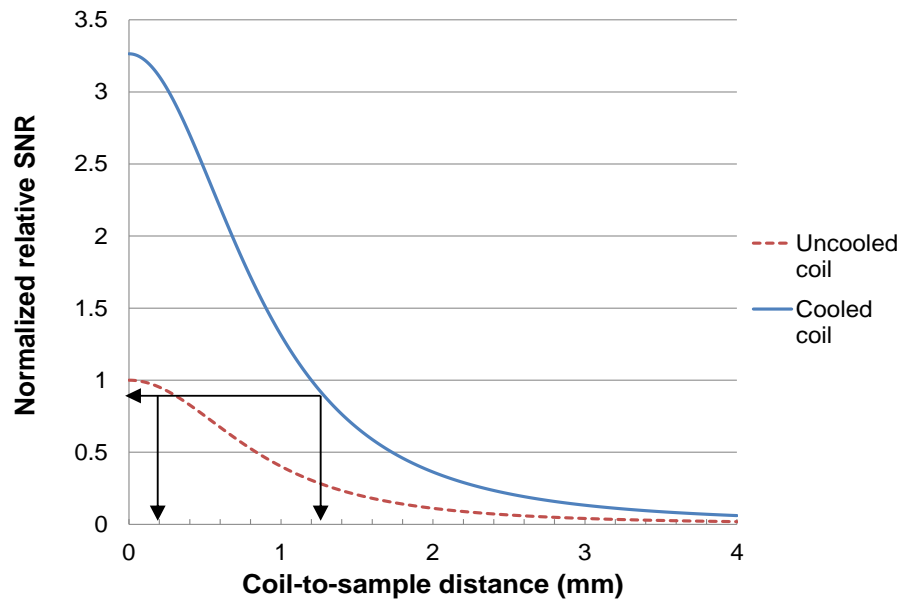
Figure 21. Simulation result of the normalized relative SNR of uncooled and cooled microcoil against the coil-to-sample distance. When the sample is placed 0.2 mm above the uncooled microcoil, the normalized relative SNR is about 0.95. To have equivalent SNR, the cooled microcoil needs to have a coil-to-sample distance of 1.25 mm or less.

Coil-to-sample distance in the current design can be reduced to 1.3 mm with relative ease by reducing the imaging surface substrate thickness from 0.3 mm to 0.2 mm and by reducing the thickness of the substrate on which the microcoil is fabricated from 0.5 mm to 0.15 mm (Figure 22). Further reduction in coil-to-sample distance needs to be achieved through reducing the depth of the nitrogen gas gap. A nitrogen gas gap reduced to 0.8 mm (currently at 1 mm) is expected to give the same relative SNR as the uncooled microcoil with the sample placed right on top of the microcoil. Thus, any further reduction in this gap will result in net SNR improvement over conventional microcoil at room temperature. One strategy for achieving a shallower nitrogen gas gap without influencing the imaging surface temperature is to utilize warm nitrogen gas

instead of room temperature nitrogen gas that is currently being used, thus improving the insulation capability of the nitrogen gas gap.
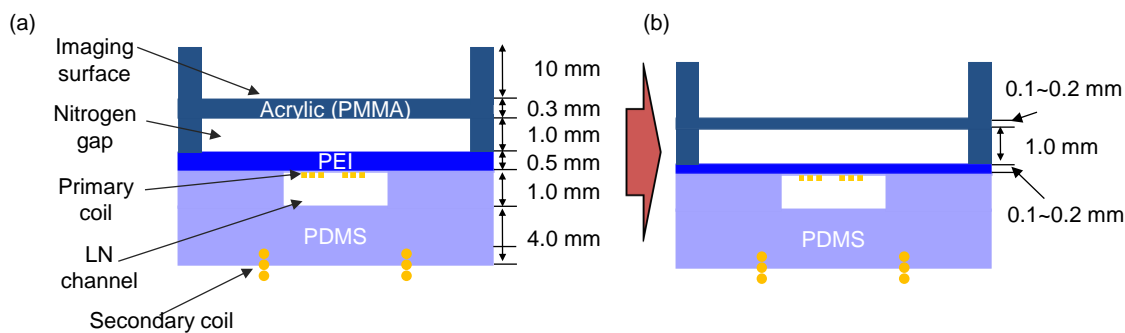
Figure 22. Optimization of the coil-to-sample distance: (a) current structure and (b) structure after optimization

For the comparison of the probe sensitivity, especially for spectroscopy applications, some investigators report the limit of detection (LOD) [78-87]. Massin *et al.* presented an LOD of 115 nMol at 300 MHz [37]. The primary coil reported here is essentially the same in structure to the coil of Massin *et al.* except for using three turns rather than two turns. Taking into account the SNR ratio between the uncooled coil with the coil-to-sample distance of 65 µm (Massin *et al.*) and the cooled microcoil with the coil-to-sample distance of 1.8 mm (our result), the estimated LOD of our coil at 300 MHz is 272 nMol. If the coil-to-sample distance is reduced further to 1.3 mm as described above, our expected LOD will be 143 nMol.

4.9. Conclusions

A microfluidically cryo-cooled spiral microcoil system with an integrated microfabricated capacitor and utilizing inductive coupling for MR microscopy has been developed and a significant improvement in Q factor was demonstrated. The use of a microfabricated parallel plate capacitor integrated with the microcoil and inductive coupling to eliminate transmission line connections allowed both the microcoil and the resonating capacitor to be enclosed by the microfluidically cryo-cooling system. This enabled localized cryo-cooling of the entire microfabricated microcoil-capacitor resonator structure without freezing the sample, while maintaining a coil-to-sample distance within a coil width of the microcoil. The system provided a 2.6 fold improvement in Q factor compared to a conventional microcoil with high-Q varactors and transmission line connection, and provided the expected improvement over our previous system that reported an improvement of 1.8 with only the coil part cryo-cooled. The result validates that cryo-cooling both the microcoil and the matching/tuning network provides a larger Q improvement than cryo-cooling only the microcoil itself, with the achieved 2.6 fold Q improvement being close to the theoretically predicted maximum Q improvement of 2.8 fold. This system may allow multiple primary microcoils to be used with a single or multiple secondary coils for effectively enabling larger or multiple fields-of-view MR microscopy.

CHAPTER V

MICROFLUIDICALLY TUNABLE RF COMPONENT

5.1. Introduction

In many RF applications, tunable RF components such as variable capacitors are one of important components [88, 89]. Mechanically tunable capacitors and electronically tunable capacitors such as semiconductor varactor diodes are typically used in the RF circuit. For magnetic resonance (MR) coil application, tunable capacitors are used as matching and tuning capacitors to match the coil impedance to 50 ohm and to tune the resonant frequency of the coil. Thus those capacitors can be adjusted from outside a magnet bore without moving the coil circuit. The mechanically tunable capacitors are not proper to be controlled remotely from the outside of the magnet bore and varactor diodes have relatively lower Q factor than fixed capacitors [90]. MEMS tunable capacitors have high Q factor, but they have low tunability due to the limitation of geometric displacement [91-102]. Alternatively, if dielectric materials of capacitors are replaced with dielectric fluids, the capacitance can be changed remotely without mechanic apparatuses. In addition, large tuning range can be obtained by selecting a fluid having a large permittivity constant and precise control of capacitance is possible by micro-controlling the position of fluids within microchannels. The fluidically tunable capacitor requires power for moving fluid only when changing capacitance, whereas varactors need a voltage to keep a capacitance, and the fluidically tunable capacitor has longer life time than MEMS tunable capacitors having moving parts.

64

The concept of using microfluidics for tunable capacitors by controlling dielectric fluids between metal plates has been reported in the past [103, 104]. However, there are very few researches on the actual RF circuit application of microfluidic tunable capacitors.

5.2. Design and Fabrication

Capacitor consists of a pair of conductors and a dielectric between the conductors. According to the parallel plate model ($C = \varepsilon A/d$), capacitance increases with area (A) and dielectric (ε), and decreases with separation (d). Unlike present variable capacitors using the change of the area and the separation, if a microfluidic channel places between the pair of the plate and supply various dielectric materials, it changes the capacitance.

Figure 23 shows the proposed microfluidically tunable capacitor structures. One is the parallel plate type (PPT) capacitor and the other is the interdigitated type (IDT) capacitor. The PPT capacitor consists of 22×5 mm^2 copper plates and a 120 µm thick PDMS microfluidic channel layer between two copper plates. As a rigid substrate for supporting the copper plates, a 30×30 mm^2 glass slide was used. The IDT capacitor has 33 fingers which are 100 µm in width and is 850 µm in length. The gap between fingers is 100 µm. A PDMS layer covers the IDT capacitor to use the finger structure of the IDT capacitor as a microfluidic channel through which a dielectric fluid flows. The entire size of the IDT capacitor is 1×1.8 mm^2.
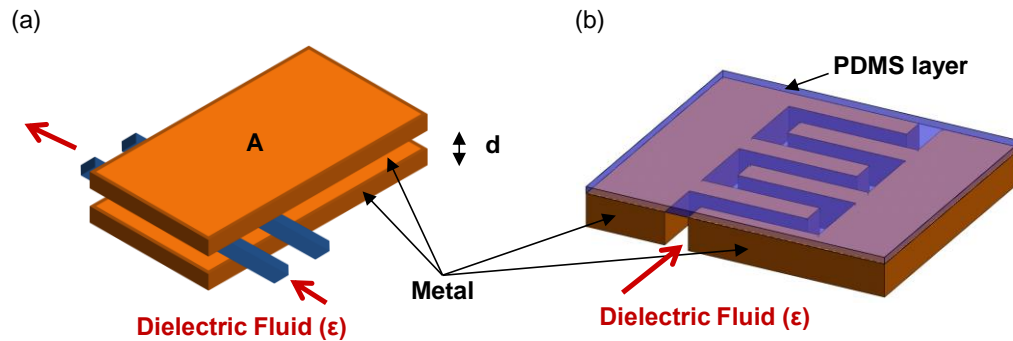
Figure 23. Concept of microfluidic tunable capacitors: (a) parallel plate type (PPT) and (b) Interdigitated type (IDT) capacitor.

Figure 24 illustrates the overall fabrication steps for the PPT and IDT capacitors. For fabricating a PPT capacitor, a 22×5 mm^2 copper tape (3M 1194, 3M, St. Paul, MN) was attached on a 50×75 mm^2 glass substrate (VWR, West Chester, PA). The copper was coated with uncured PDMS using a spin coater at 1000 RPM for 30 sec and placed in an oven to cure PDMS. Microfluidic channels were etched using a laser micromachining equipment (PLS 6.120D, Universal Laser Systems, Inc., Scottsdale, AZ) with a 1% power, 24% speed, and 400 pulse per inch (PPI) resolution condition. Then, another PDMS coated copper plate substrate was prepared and they bonded to each other using oxygen plasma treatment.

For fabricating a PPT capacitor, a chromium/copper (30/300 nm) seed layer was deposited on a 1 mm thick and 50×75 mm^2 glass substrate using an electron-beam evaporator. Then, a 35 µm thick photoresist (NR21-20000P, Futurrex Inc., Franklin, NJ) was spun, and the rectangular shape of the parallel plate capacitor was defined using a photolithography process. Following photolithography, 25 µm of copper was electroplated using a copper sulfate solution ($CuSO_4 : H_2SO_4 : H_2O$ = 250 g : 25 ml : 1 L)

at a current density of 10 mA/cm^2. The photoresist was removed by acetone and the chromium/copper seed layer was etched by chrome etchant (TFE, Transene Company Inc., Danvers, MA) and copper etchant (CE-100, Transene Company Inc). Finally, a 30 μm thick PDMS layer was placed on top of the copper structure to seal it and make a microfluidic channel. Figure 25 shows the fabricated PPT and IDT capacitors.
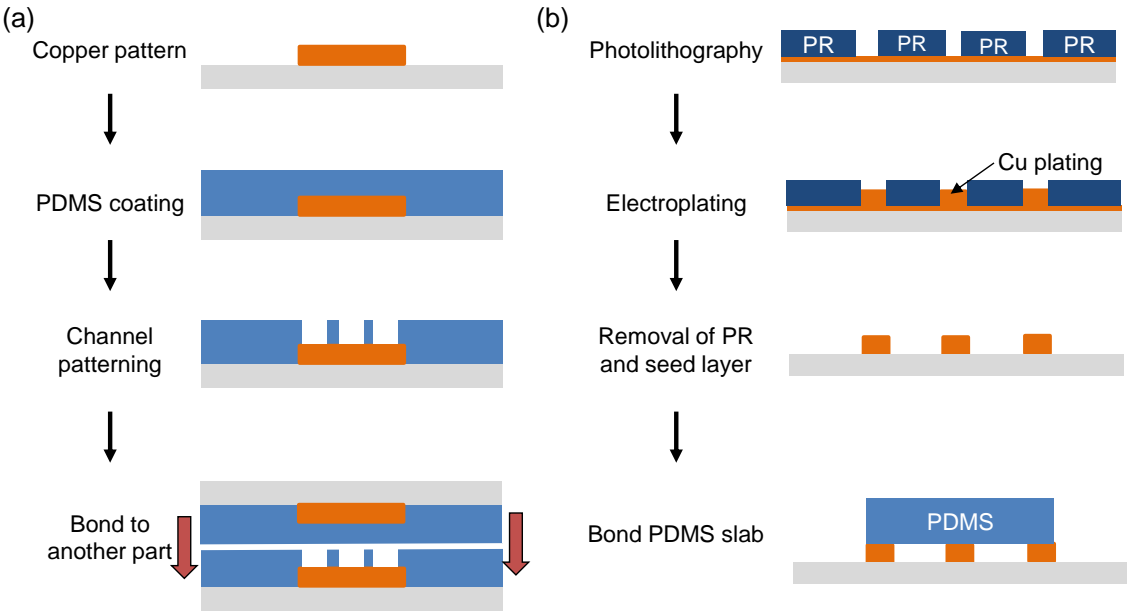
Figure 24. Illustration of the fabrication processes for microfluidic tunable capacitors: (a) the PPT capacitor and (b) the IDT capacitor.
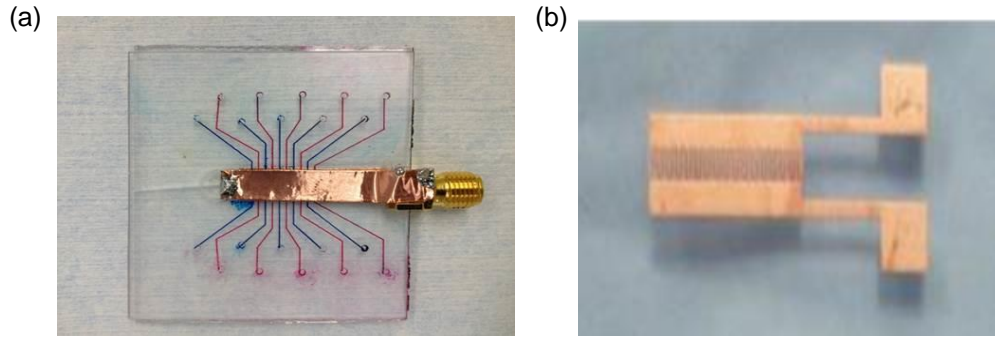
Figure 25. Pictures of the fabricated PPT capacitor and the IDT capacitor. (a) The PPT capacitor's microchannels were filled with blue and red inks to show that the microchannels are isolated to selectively fill the microchannel to vary the capacitance. (b) After placing a PDMS layer on top of it, the interdigitated finger becomes single fluidic channel.

5.3. Characterization of Microfluidically Tunable Capacitors

DI water ($\varepsilon = 80$) and mineral oil ($\varepsilon = 3$) were selected as dielectric fluids for the PPT capacitor and the IDT capacitor. At 200 MHz, capacitance of the capacitors while filling with dielectric fluids was measured using a vector network analyzer (HP 4195A) and the equivalent series resistance (ESR) to specify the Q of capacitors. A vector network analyzer with impedance test kit (HP 41951A) was used and series RC model was used as described in the thesis of Richard F. Godley [77].

5.3.1. Parallel Plate Type (PPT) Capacitor

The capacitance of the PPT capacitor changed linearly from 40.1 pF to 53.1 pF (32.4% tunability) when injecting DI water into one by one microfluidic channel (Figure 26a). When using mineral oil, the capacitance varied linearly from 40.1 pF to 41.5 pF (3.4% tunability). Due to higher dielectric constant of DI water than the one of mineral oil, the

range of capacitance using DI water is larger than the mineral oil. The measured capacitance is close to the expected capacitance based on a parallel capacitor model (C = εA/d), from 37.8 pF to 47.1 pF (24.6% tunability) when using DI water. Figure 26b shows the measured Q of the PPT capacitor. While the Q of the PPT capacitor filled with DI water changed from 82 to 89, the Q of the capacitor filled with oil changed from 84 to 106. The ESR of the capacitor changed 0.6 ohm before and after filling DI water and the ESR of the capacitor changed 0.5 ohm when using oil. The variation of the ESR is similar when using water and mineral oil, but the variation of capacitance when using mineral oil is smaller than the one when using DI water. Thus the variation of Q factor when using mineral oil is larger than the one when using DI water.
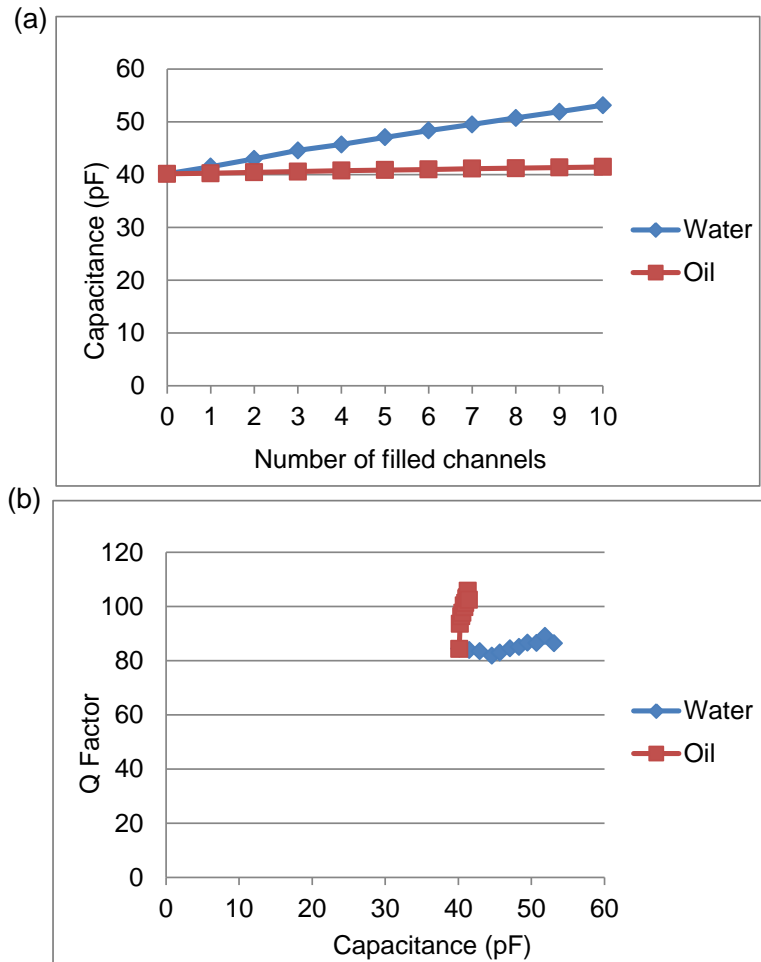
Figure 26. (a) Capacitance of the PPT capacitor when filling water and mineral oil as dielectric fluid through the microchannels placed between two metal plates and (b) Q factor of the PPT capacitor.

5.3.2. Interdigitated Type (IDT) Capacitor

The capacitance of the IDT capacitor changed linearly from 3.2 pF to 24.1 pF (653% tunability) when injecting DI water through the microfluidic channels in the IDT capacitor (Figure 27a). When using mineral oil, the capacitance varied linearly from 3.2 pF to 4 pF (25% tunability). To increase the range of capacitance, barium strontium titanate (BSTO) material was tested because it can reach more than 250 in dielectric

constant and it is used for RF components [105]. To flow BSTO powder through the microfluidic channel, mineral oil was used as a fluidic solution to suspend and deliver BSTO powders through the microfluidic channel. 1 wt% concentration was used to prevent the precipitation of BSTO powders and the clog of the microfluidic channel. However, the concentration of BSTO provides only from 3.2 pF to 5.3 pF (65.6% tunability), similar range of capacitance with the one using mineral oil. To achieve higher range of capacitance, the concentration should increase more without the precipitation of BSTO powders.

Figure 27b shows the measured Q of the IDT capacitor. In addition, Q factor of high-Q varactor (MV34009, Microsemi Microwave Products, Lowell, MA) [77] was added into the graph to compare it to the IDT capacitor. As similar as the PPT capacitor, the variation of Q factor when using mineral oil is larger than the one when using water. However, Q factor when using mineral oil and BSTO mixture is higher than the one of high-Q varactor. When using water, the IDT capacitor has wider range of capacitance and more constant Q factor than the high-Q varactor.

Finite element method (FEM)-based models were implemented using commercially available FEM software (HFSS, ANSYS Inc., Canonsburg, PA) with the help of Shuli Li in Dr. Gregory H. Huff lab. Relative permittivity of 80, 3 and 2.5 were selected for DI water, mineral oil and PDMS, respectively.

Figure 28 shows the comparison between the measurement data and the simulation data. When using mineral oil (Figure 28a) and water (Figure 28b), the

electromagnetic simulation shows the capacitance increases linearly according to the filling percentage of dielectric fluid.
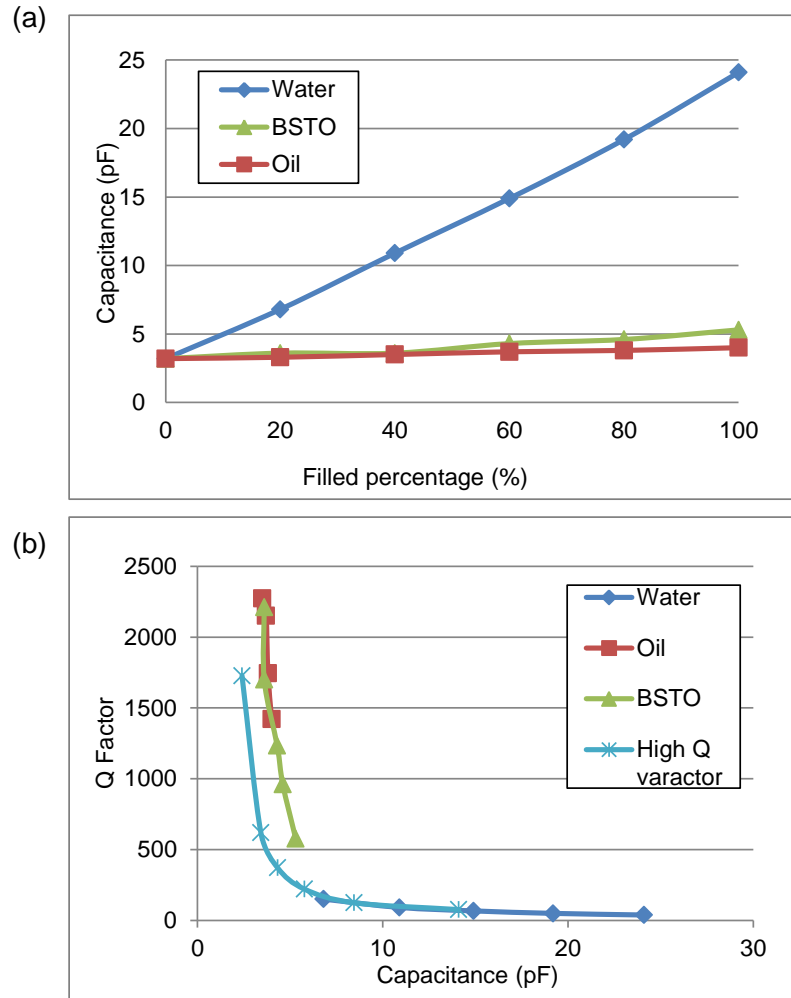
Figure 27. (a) Capacitance of the IDT capacitor when filling water, mineral oil and BSTO-oil mixture as dielectric fluid through the capacitor and (b) Q factor of the IDT capacitor and a high-Q varactor.
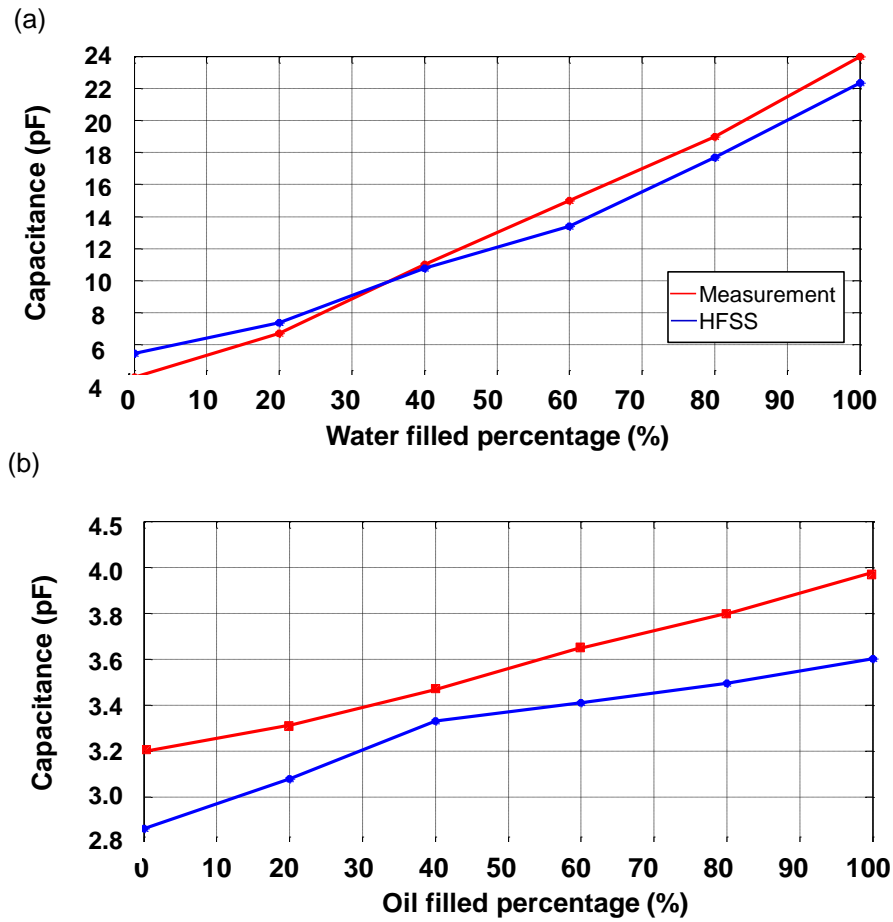
Figure 28. FEM simulation result of the capacitance when flowing (a) DI water and (b) mineral oil through the microfluidic channel of the IDT capacitor. Red line is the measurement data and blue line is the simulation result.

5.4. Integration with a Single MR Planar Pair Coil

The microfluidically tunable capacitor was integrated with a SEA coil which was described in chapter 2. To tune and match the coil, two tunable capacitors were connected to the coil in series and in parallel. While injecting a dielectric fluidic into the capacitors, the resonant frequency of the coil was characterized and its Q factor was measured.

The two IDT capacitors were integrated with a SEA coil to tune and match it (Figure 29a). The SEA coil was tuned at 200 MHz and matched at 50 ohm using mineral oil through the IDT capacitors, the measured Q was 26, similar to the Q (=28) of another SEA coil integrated with high-Q varactors. Figure 29b shows that Q of the SEA coil integrated with IDT capacitors is constant from 24 to 28 while tuning it at ten different resonant frequencies (from 155 MHz to 235 MHz) with 50 ohm matching.

(a)

Tuning/Matching	Q factor of tuned and matched coil (200MHz)
Microfluidically Tunable capacitor (IDT type)	26
High-Q varactor	28

(b)
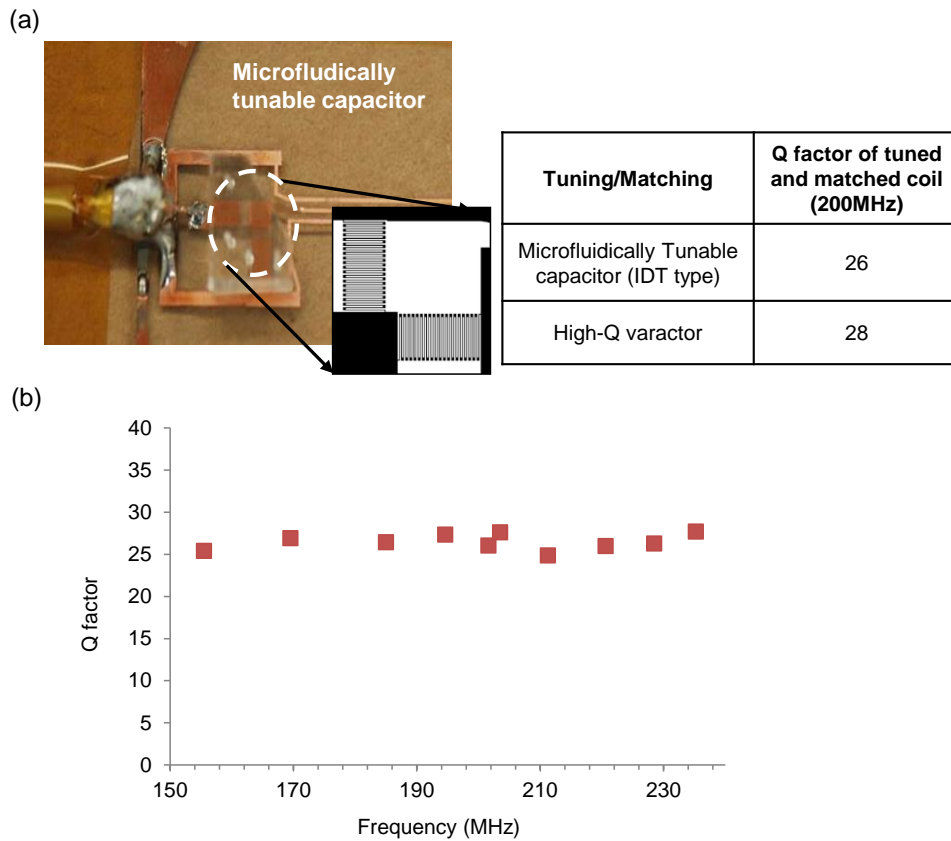
Figure 29. (a) IDT capacitors integrated with a 5 cm long SEA coil. One capacitor was used to tune the coil and the other one was used to match the coil to 50 ohm. The measured Q of the SEA coil integrated with IDT capacitors was similar to the Q of the SEA coil integrated with high-Q varactors. (b) The Q of the SEA coil was constant while tuning it at 10 different frequencies.

5.5. Integration with Multiple MR Planar Pair Coil Array

To expand the application of the microfluidically tunable capacitor to an array of multiple MR planar coils, an array of three MR planar pair coils integrated with the tunable capacitor was designed (Figure 30). Three MR planar pair coils had different inductance so that different capacitances were required to tune them at sample resonant frequency. As a proof of concept, the array of SEA coils had one tunable capacitor for tuning it. To select a SEA coil to be tuned among three SEA coils, a pneumatic valve was integrated in front of the tunable capacitor. It worked as a switch for microfluidic channel and it is normally closed, but it is open when negative pressure is applied to the pneumatic valve. A dielectric fluid for changing the capacitance of the tunable capacitor was constantly injected through the inlet of the microfluidic channels on the SEA coil array using a syringe pump. The dielectric fluid flowed through the bypass channel placed at the left of each SEA coil when the pneumatic valve was close, and the fluid flowed through the tunable capacitor when a selected pneumatic valve was open. When the selected SEA coil was tuned at a target resonant frequency, the pneumatic valve was close again and the fluid stopped flowing through the microchannel in the tunable capacitor and flowed through the bypass channel. Thus the resonant frequency of the SEA was maintained. Then other SEA coils were tuned using same procedure. Once all SEA coils were tuned at the target resonant frequency, the syringe pump to flow dielectric fluid was turned off and no more fluid flowed through the entire microfluidic channels. To measure the resonant frequency of the coil, dual probes were used with an S_{21} transmission-type measurement.

75
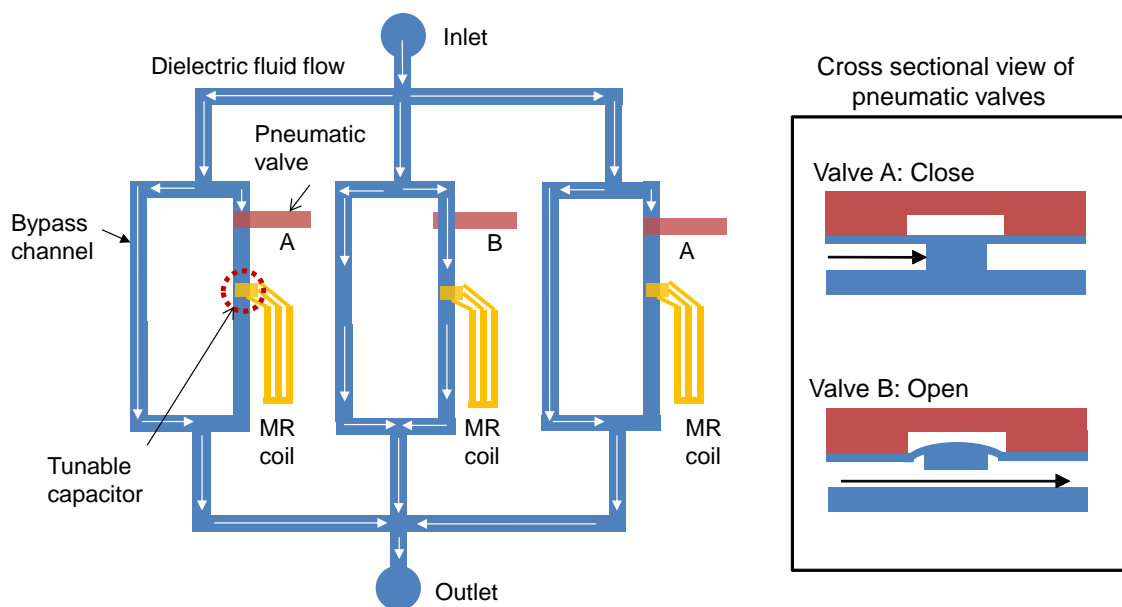
Figure 30. Concept of an array of MR coils integrated with microfluidically tunable capacitors. The MR coil to be tuned was selected by the pneumatic valves.

Figure 31a shows that all pneumatic valves were closed and dielectric fluid flowed through bypass channels, not through the microchannels in the IDT capacitors. Thus no coil could be tuned at this moment. When the pneumatic valve at the middle coil of three SEA coils was open, the coil was selected to change the resonant frequency of it. Figure 31b shows that the middle SEA coil was successfully selected by the pneumatic valve and the dielectric fluid flowed through the microchannels in the IDT capacitor integrated with the coil. While the capacitance of the IDT capacitor changed, the resonant frequency of the middle coil shifted from 350 MHz to 186 MHz.
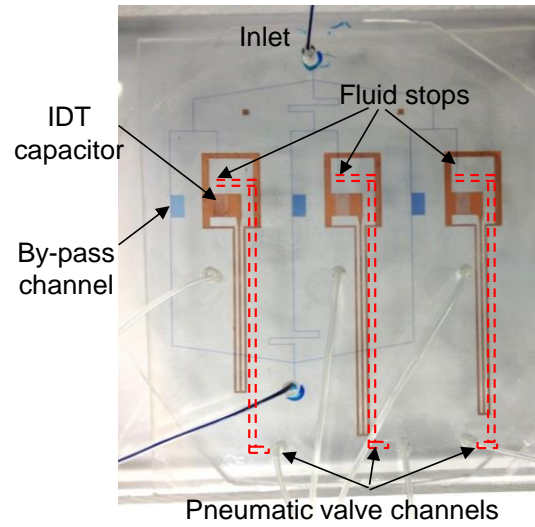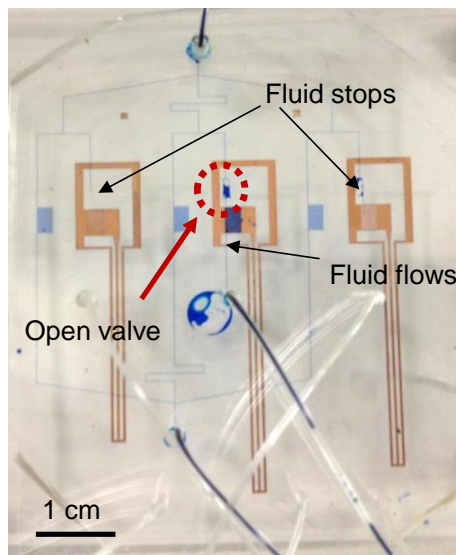
Figure 31. (a) The array of SEA coils integrated with IDT capacitors when all pneumatic valves were close. The dielectric fluid (blue ink) flowed only through bypass channels, not through the channel in IDT capacitors. (b) The pneumatic valve for the middle coil of the three coils was open and the dielectric fluid flowed through the channel in the IDT capacitor.

5.6. Conclusions

Two microfluidically tunable capacitors have been developed and an array of MR coils integrated with tunable capacitors was demonstrated as a proof of concept. Wide range of capacitance in the PPT capacitor and the IDT capacitor was obtained when using a high dielectric fluid such as DI water. In the PPT capacitor, the capacitance tunability was 32.4% when using water and 3.4% when using mineral oil. In the IDT capacitor, the capacitance tunability was 653% when using water and 25% tunability when using mineral oil. When BSTO-oil mixture was used, the tunability was 65.6%. A MR SEA coil integrated with two IDT capacitors was successfully tuned at the frequency between 155 MHz and 235 MHz and matched to 50 ohm. An array of three SEA coils integrated with IDT capacitors was demonstrated and the each coil could be tuned using one dielectric fluid source and three pneumatic valves. The developed microfluidically tunable capacitors have high tunability and can be tuned from outside a magnet bore once the coil system using the tunable capacitors is loaded in the bore.

CHAPTER VI

FUTURE WORK AND CONCLUSIONS

This study has described the culmination of efforts on integrated microfluidic system for magnetic resonance imaging (MR) for locally cryo-cooling small copper coils to improve the signal to noise ratio (SNR) of MR imaging without freezing samples to be imaged and microfluidically tuning RF capacitors to have the MR coil with wide tuning range and high Q.

A single planar pair coil was integrated with a cryo-cooling channel and the nitrogen gas gap as a wall of a cryostat to prevent the sample from being frozen. The substrate of the coil and the cryo-cooling channel was made of a polymer having lower thermal conductivity to minimize the effect of thermal transfer from the cryo-cooling channel to the entire coil system. The MR images were obtained with the cryo-cooled coil system in 4.7T MR system and observed an average SNR enhancement of 1.5 fold. The current system is able to cryo-cool the MR coil and obtain MR images for 1 hr due to the volume limit of the liquid nitrogen dewar (20 L). Using a larger dewar is one solution to achieve a long imaging time over 1 hr. Results of this cryo-cooled single planar coil system were published in a journal paper [61].

To increase SNR more, coil-to-sample distance (2.1 mm in the current setup) should be minimized because the coil for Single Echo Acquisition (SEA) imaging has a narrow width and a short imaging depth, equal to the width of the SEA coil approximately (2 mm in the current design). Coil-to-sample distance can be reduced to

1.3 mm with relative ease by reducing the imaging surface substrate thickness from 0.3 mm to 0.2 mm and by reducing the thickness of the substrate on which the microcoil is fabricated from 0.5 mm to 0.15 mm. In addition, 1 mm nitrogen gas gap can be shallower without influencing the imaging surface temperature by utilizing warm nitrogen gas instead of room temperature nitrogen gas. If coil-to-sample distance can be reduced without freezing image samples, the single cryo-cooled SEA coil system can allow higher quality of SEA imaging than the SEA coil system at room temperature.

An array of multiple MR planar pair coils for implementing SEA imaging, one of rapid imaging techniques, was demonstrated while cryo-cooling the entire array of SEA coils to increase SNR of SEA imaging. The microfluidically cryo-cooling method was applied to an array of SEA coils. When the coil array was cryo-cooled, Q of each coil in the array increased 1.8 fold, enabling similar SNR improvement (1.5 fold) of the single microfluidically cryo-cooled planar coil system. The current limitation is that the imaging time is 1 hr because the imaging surface becomes below 0℃ after 1 hr of cryo-cooling. To solve the obstacle for SEA imaging with the cryo-cooled array of SEA coils system, and optimization of the width of cryo-cooling channels and the distance between the cryo-cooling channels is required in further study.

Measured Q enhancement was lower than expected Q enhancement when cryo-cooling the copper MR coil and further investigation revealed that the resistance of the matching/tuning network was higher than the microcoil. To cryo-cool the tuning network, on-chip capacitor was microfabricated with the microcoil and inductive coupling was investigated to eliminate transmission line connections allowing both the

microcoil and the resonating capacitor to be enclosed by the microfluidically cryo-cooling system. Microfabricated microcoil-capacitor resonator was locally cryo-cooled without freezing the sample. The system provided a 2.6 fold improvement in Q factor compared to a conventional microcoil with high-Q varactors and transmission line connection, and provided the expected improvement over our previous system that reported an improvement of 1.8 with only the coil part cryo-cooled. To obtain better SNR than the one of the uncooled microcoil with 0.2 mm of coil-to-sample distance, the cryo-cooled microcoil in current setup needs to have a coil-to-sample distance of 1.15 mm or less. Coil-to-sample distance can be reduced to 1.3 mm with relative ease by using same method to reduce coil-to-sample distance of the cryo-cooled planar pair coil system. However, further study is required to reduce the distance below 1.15 mm. This system may allow multiple primary microcoils to be used with a single or multiple secondary coils for effectively enabling larger or multiple fields-of-view MR microscopy.

A microfluidically tunable capacitor with high tunability and high Q was demonstrated as an alternative of semiconductor varactors diodes and MEMS capacitors. Developed microfluidically tunable capacitors were successfully integrated with a single MR coil and able to tune the coil and match it to 50 ohm. Q of the coil using microfluidically tunable capacitors is high as much as the one of the coil using high-Q varactors while the coil using microfluidically tunable capacitors has wider range of tunability. To implement the microfluidically tunable capacitor to an array of multiple SEA coils, a microfluidic channel system with pneumatic valves to select a SEA coil to

tune it was demonstrated as a proof of concept. The copper structure of the array of three SEA coils integrated with an interdigitated type (IDT) capacitor was combined with the PDMS microfluidic channel with pneumatic valves. A dielectric fluid flowed through the microfluidic channels in the selected IDT capacitor integrated with the SEA coil to be tuned. The further optimized microfluidically tunable capacitor with higher Q and large tunability is potentially able to be used as the matching/tuning capacitors for an array of MR coils requiring high Q.

REFERENCES

[1]   J. G. v. Heteren, T. W. James, and L. C. Bourne, "Thin Film High Temperature Superconducting RF Coils for Low Field MRI," *Magnetic Resonance in Medicine,* vol. 32, pp. 396-400, 1994.

[2]   E. Harel, "Magnetic Resonance Detection: Spectroscopy and Imaging of Lab-On-a-Chip," *Lab on a Chip,* vol. 9, pp. 17-23, 2009.

[3]   R. D. Black, P. B. Roemer, and O. M. Mueller, "Electronics for a High Temperature Superconducting Receiver System for Magnetic Resonance Microimaging," *IEEE Transactions on Biomedical Engineering,* vol. 41, pp. 195-197, 1994.

[4]   A. C. Wright, H. K. Song, and F. W. Wehrli, "In Vivo MR Micro Imaging With Conventional Radiofrequency Coils Cooled to 77°K," *Magnetic Resonance in Medicine,* vol. 43, pp. 163-169, 2000.

[5]   J.-C. Ginefri, L. Darrasse, and P. Crozat, "High-Temperature Superconducting Surface Coil for In Vivo Microimaging of the Human Skin," *Magnetic Resonance in Medicine,* vol. 45, pp. 376-382, 2001.

[6]   D. Ratering, C. Baltes, J. Nordmeyer-Massner, D. Marek, and M. Rudin, "Performance of a 200-Mhz cryogenic RF probe designed for MRI and MRS of the Murine Brain," *Magnetic Resonance in Medicine,* vol. 59, pp. 1440-1447, 2008.

[7]   K. P. Pruessmann, M. Weiger, M. B. Scheidegger, and P. Boesiger, "SENSE: Sensitivity Encoding for fast MRI," *Magnetic Resonance in Medicine,* vol. 42, pp. 952-962, 1999.

[8]   J. A. Bankson, M. A. Griswold, S. M. Wright, and D. K. Sodickson, "SMASH Imaging with an Eight Element Multiplexed RF Coil Array," *Magnetic Resonance Materials in Physics, Biology and Medicine,* vol. 10, pp. 93-104, 2000.

[9]   M. P. McDougall and S. M. Wright, "64-Channel Array Coil for Single Echo Acquisition Magnetic Resonance Imaging," *Magnetic Resonance in Medicine,* vol. 54, pp. 386-392, 2005.

[10]   S. M. Wright and M. P. McDougall, "Single Echo Acquisition MRI Using RF Encoding," *NMR in Biomedicine,* vol. 22, pp. 982-993, 2009.

[11]   R. R. Tummala, *Fundamentals of Microsystems Packaging*. New York: McGraw-Hill, 2001.

[12]   D. B. Tuckerman and F. W. Pease, "High-Performance Heat Sinking for VLSI," *IEEE Electron Device Letters,* vol. 2, pp. 126-129, 1981.

[13]   J. Darabi, M. M. Ohadi, and D. DeVoe, "An Electrohydrodynamic Polarization Micropump for Electronic Cooling," *Journal of Microelectromechanical Systems,* vol. 10, pp. 98-106, 2001.

[14]   Y. Yokoyama, M. Takeda, T. Umemoto, and T. Ogushi, "Thermal Micro Pumps for a Loop-type Micro Channel," *Sensors and Actuators A,* vol. 111, pp. 123-128, 2004.

[15]   E. N. Wang, L. Z. L. J. J.-M. Koo, J. G. Maveety, E. A. Sanchez, K. E. Goodson, and T. W. Kenny, "Micromachined Jets for Liquid Impingement Cooling of VLSI Chips," *Journal of Microelectromechanical Systems,* vol. 13, pp. 833-842, 2004.

[16]   J. Darabi and H. Wang, "Development of an Electrohydrodynamic Injection Micropump and Its Potential Application in Pumping Fluids in Cryogenic

Cooling Systems," *Journal of Microelectromechanical Systems,* vol. 14, pp. 747-755, 2005.

[17]   S. Grohmann, R. Herzog, T. O. Niinikoski, B. Perea-Solano, H. Quack, G. Vögele, and E. Wobst, "Development of a Miniature Cryogenic Fluid Circuit and a Cryogenic Micropump," *Cryogenics,* vol. 45, pp. 432-438, 2005.

[18]   D. R. Lide, *CRC Handbook of Chemistry and Physics*, 90th ed. Boca Raton, FL: CRC Press/Taylor and Francis, 2010.

[19]   J. S. Hyde, W. Froncisz, A. Jesmanowicz, and J. B. Kneeland, "Planar-pair Local Coils for High-resolution Magnetic Resonance Imaging, Particularly of the Temporomandibular Joint," *Medical Physics,* vol. 13, pp. 1-7, 1986.

[20]   R. S. Kane, S. Takayama, E. Ostuni, D. E. Ingber, and G. M. Whitesides, "Patterning Proteins and Cells Using Soft Lithography," *Biomaterials,* vol. 20, pp. 2363-2376, 1999.

[21]   S. Bhattacharya, A. Datta, J. M. Berg, and S. Gangopadhyay, "Studies on Surface Wettability of Poly(dimethyl) Siloxane (PDMS) and Glass Under Oxygen-Plasma Treatment and Correlation with Bond Strength," *Journal of Microelectromechanical Systems,* vol. 14, pp. 590-597, 2005.

[22]   B. H. Jo, L. M. Van Lerberghe, K. M. Motsegood, and D. J. Beebe, "Three-dimensional Micro-channel Fabrication in Polydimethylsiloxane (PDMS) Elastomer," *Journal of Microelectromechanical Systems,* vol. 9, pp. 76-81, 2000.

[23]   Y. Park, C. Koo, H.-Y. Chen, A. Han, and D. H. Son, "Ratiometric Temperature Imaging Using Environment-insensitive Luminescence of Mn-doped Core-shell Nanocrystals," *Nanoscale,* vol. 5, pp. 4944-4950, 2013.

[24]   R. E. Collin, *Foundations for Microwave Engineering*, 2nd ed. New York: Wiley-IEEE Press, 2001.

[25] J. W. Carlson and T. Minemura, "Imaging Time Reduction Through Multiple Receiver Coil Data Acquisition and Image Reconstruction," *Magnetic Resonance in Medicine,* vol. 29, pp. 681-687, 1993.

[26] D. Kwiat, S. Einav, and G. Navon, "A Decoupled Coil Detector Array for Fast Image Acquisition in Magnetic Resonance Imaging," *Medical Physics,* vol. 18, pp. 251-265, 1991.

[27] J. B. Ra and C. Y. Rim, "Fast Imaging Using Subencoding Data Sets from Multiple Detectors," *Magnetic Resonance in Medicine,* vol. 30, pp. 142-145, 1993.

[28] P. B. Roemer, W. A. Edelstein, C. E. Hayes, S. P. Souza, and O. M. Mueller, "The NMR Phased Array," *Magnetic Resonance in Medicine,* vol. 16, pp. 192-225, 1990.

[29] M. Hutchinson and U. Raff, "Fast MRI Data Acquisition Using Multiple Detectors," *Magnetic Resonance in Medicine,* vol. 6, pp. 87-91, 1988.

[30] J. S. Hyde, W. Froncisz, A. Jesmanowicz, and J. B. Kneeland, "Simultaneous Image Acquisition from the Head (or body) Coil and a Surface Coil," *Magnetic Resonance in Medicine,* vol. 6, pp. 235-239, 1988.

[31] D. K. Sodickson and W. J. Manning, "Simultaneous Acquisition of Spatial Harmonics (SMASH): Fast Imaging with Radiofrequency Coil Arrays," *Magnetic Resonance in Medicine,* vol. 38, pp. 591-603, 1997.

[32] W. E. Kyriakos, L. P. Panych, D. F. Kacher, C.-F. Westin, S. M. Bao, R. V. Mulkern, and F. A. Jolesz, "Sensitivity Profiles from an Array of Coils for Encoding and Reconstruction in Parallel (SPACE RIP)," *Magnetic Resonance in Medicine,* vol. 44, pp. 301-308, 2000.

[33]   J. A. de Zwart, P. J. Ledden, P. van Gelderen, J. Bodurka, R. Chu, and J. H. Duyn, "Signal-to-noise Ratio and Parallel Imaging Performance of a 16-channel Receive-only Brain Coil Array at 3.0 Tesla," *Magnetic Resonance in Medicine,* vol. 51, pp. 22-26, 2004.

[34]   J. R. Porter, S. M. Wright, and A. Reykowski, "A 16-element phased-array head coil," *Magnetic Resonance in Medicine,* vol. 40, pp. 272-279, 1998.

[35]   Y. Zhu, C. J. Hardy, D. K. Sodickson, R. O. Giaquinto, C. L. Dumoulin, G. Kenwood, T. Niendorf, H. Lejay, C. A. McKenzie, M. A. Ohliger, and N. M. Rofsky, "Highly Parallel Volumetric Imaging with a 32-element RF Coil Array," *Magnetic Resonance in Medicine,* vol. 52, pp. 869-877, 2004.

[36]   D. L. Olson, T. L. Peck, A. G. Webb, R. L. Magin, and J. V. Sweedler, "High-Resolution Microcoil 1H-NMR for Mass-Limited, Nanoliter-Volume Samples," *Science,* vol. 270, pp. 1967-1970, 1995.

[37]   C. Massin, F. Vincent, A. Homsy, K. Ehrmann, G. Boero, P. A. Besse, A. Daridon, E. Verpoorte, N. F. de Rooij, and R. S. Popovic, "Planar Microcoil-based Microfluidic NMR Probes," *Journal of Magnetic Resonance,* vol. 164, pp. 242-255, 2003.

[38]   J. H. Walton, J. S. de Ropp, M. V. Shutov, A. G. Goloshevsky, M. J. McCarthy, R. L. Smith, and S. D. Collins, "A Micromachined Double-Tuned NMR Microprobe," *Analytical Chemistry,* vol. 75, pp. 5030-5036, 2003.

[39]   S. Eroglu, B. Gimi, B. Roman, G. Friedman, and R. L. Magin, "NMR Spiral Surface Microcoils: Design, Fabrication, and Imaging," *Concepts in Magnetic Resonance Part B: Magnetic Resonance Engineering,* vol. 17B, pp. 1-10, 2003.

[40]   H. Wensink, F. Benito-Lopez, D. C. Hermes, W. Verboom, H. J. G. E. Gardeniers, D. N. Reinhoudt, and A. van den Berg, "Measuring Reaction

Kinetics in a Lab-on-a-chip by Microcoil NMR," *Lab on a Chip,* vol. 5, pp. 280-284, 2005.

[41]   K. Ehrmann, N. Saillen, F. Vincent, M. Stettler, M. Jordan, F. M. Wurm, P.-A. Besse, and R. Popovic, "Microfabricated Solenoids and Helmholtz Coils for NMR Spectroscopy of Mammalian Cells," *Lab on a Chip,* vol. 7, pp. 373-380, 2007.

[42]   V. Badilita, K. Kratt, N. Baxan, M. Mohmmadzadeh, T. Burger, H. Weber, D. v. Elverfeldt, J. Hennig, J. G. Korvink, and U. Wallrabe, "On-chip Three Dimensional Microcoils for MRI at the Microscale," *Lab on a Chip,* vol. 10, pp. 1387-1390, 2010.

[43]   H. Weber, N. Baxan, D. Paul, J. Maclaren, D. Schmidig, M. Mohammadzadeh, J. Hennig, and D. von Elverfeldt, "Microcoil-based MRI: Feasibility Study and Cell Culture Applications Using a Conventional Animal System," *Magnetic Resonance Materials in Physics, Biology and Medicine,* vol. 24, pp. 137-145, 2011.

[44]   H. Ryan, S.-H. Song, A. Zaß, J. Korvink, and M. Utz, "Contactless NMR Spectroscopy on a Chip," *Analytical Chemistry,* vol. 84, pp. 3696-3702, 2012.

[45]   O. G. Gruschke, N. Baxan, L. Clad, K. Kratt, D. von Elverfeldt, A. Peter, J. Hennig, V. Badilita, U. Wallrabe, and J. G. Korvink, "Lab on a Chip Phased-array MR Multi-platform Analysis System," *Lab on a Chip,* vol. 12, pp. 495-502, 2012.

[46]   C. Massin, G. Boero, F. Vincent, J. Abenhaim, P. A. Besse, and R. S. Popovic, "High-Q Factor RF Planar Microcoils for Micro-scale NMR Spectroscopy," *Sensors and Actuators A: Physical,* vol. 97-98, pp. 280-288, 2002.

[47]   K. Ehrmann, K. Pataky, M. Stettler, F. M. Wurm, J. Brugger, P.-A. Besse, and R. Popovic, "NMR Spectroscopy and Perfusion of Mammalian Cells Using Surface Microprobes," *Lab on a Chip,* vol. 7, pp. 381-383, 2007.

[48]   G. Boero, J. Frounchi, B. Furrer, P.-A. Besse, and R. S. Popovic, "Fully Integrated Probe for Proton Nuclear Magnetic Resonance Magnetometry," *Review of Scientific Instruments,* vol. 72, pp. 2764-2768, 2001.

[49]   S. Eroglu, G. Friedman, and R. L. Magin, "Estimate of Losses and Signal-to-noise Ratio in Planar Inductive Micro-coil Detectors Used for NMR," *IEEE Transactions on Magnetics,* vol. 37, pp. 2787-2789, 2001.

[50]   S. E. Hurlston, W. W. Brey, S. A. Suddarth, and G. A. Johnson, "A High-temperature Superconducting Helmholtz Probe for Microscopy at 9.4 T," *Magnetic Resonance in Medicine,* vol. 41, pp. 1032-1038, 1999.

[51]   J. Wosik, F. Wang, L. M. Xie, M. Strikovski, M. Kamel, K. Nesteruk, M. Bilgen, and P. A. Narayana, "High-Tc Superconducting Surface Coil for 2 Tesla Magnetic Resonance Imaging of Small Animals," *IEEE Transactions on Applied Superconductivity,* vol. 11, pp. 681-684, 2001.

[52]   J. Wosik, X. Lei-Ming, K. Nesteruk, X. Lian, J. A. Bankson, and J. D. Hazle, "Superconducting Single and Phased-array Probes for Clinical and Research MRI," *IEEE Transactions on Applied Superconductivity,* vol. 13, pp. 1050-1055, 2003.

[53]   D. Ratering, C. Baltes, J. Nordmeyer-Massner, D. Marek, and M. Rudin, "Performance of a 200-MHz Cryogenic RF Probe Designed for MRI and MRS of the Murine Brain," *Magnetic Resonance in Medicine,* vol. 59, pp. 1440-1447, 2008.

[54]   W. W. Brey, A. S. Edison, R. E. Nast, J. R. Rocca, S. Saha, and R. S. Withers, "Design, construction, and validation of a 1-mm triple-resonance high-temperature-superconducting probe for NMR," *Journal of Magnetic Resonance,* vol. 179, pp. 290-293, 2006.

[55]   P. Styles, N. F. Soffe, C. A. Scott, D. A. Crag, F. Row, D. J. White, and P. C. J. White, "A high-resolution NMR probe in which the coil and preamplifier are cooled with liquid helium," *Journal of Magnetic Resonance,* vol. 60, pp. 397-404, 1984.

[56]   R. Black, T. Early, P. Roemer, O. Mueller, A. Mogro-Campero, L. Turner, and G. Johnson, "A high-temperature Superconducting Receiver for Nuclear Magnetic Resonance Microscopy," *Science,* vol. 259, pp. 793-795, 1993.

[57]   Q. Y. Ma, K. C. Chan, D. F. Kacher, E. Gao, M. S. Chow, K. K. Wong, H. Xu, E. S. Yang, G. S. Young, J. R. Miller, and F. A. Jolesz, "Superconducting RF Coils for Clinical MR Imaging at Low Field," *Academic Radiology,* vol. 10, pp. 978-987, 2003.

[58]   J. Wosik, L. Xue, L.-M. Xie, M. R. Kamel, K. Nesteruk, and J. A. Bankson, "Superconducting Array for High-field Magnetic Resonance Imaging," *Applied Physics Letters,* vol. 91, p. 183503, 2007.

[59]   C. Koo, M. A. Carillo, M. P. McDougall, S. M. Wright, and A. Han, "A Cryo-Cooling Microfluidic Device for Magnetic Resonance (MR) Microscopy System," in *μTAS 2010, The 14th International Conference on Miniaturized Systems for Chemistry and Life Sciences*, Groningen, The Netherlands, 2010, pp. 614-616.

[60]   C. Koo, R. Godley, M. P. McDougall, S. M. Wright, and A. Han, "Microfluidically Cryo-cooled Inductively Coupled Spiral Microcoils for MR

Microscopy," in *μTAS 2011, The 15th International Conference on Miniaturized Systems for Chemistry and Life Sciences*, Seattle, USA, 2011, pp. 1311-1313.

[61]   C. Koo, R. F. Godley, J. Park, M. P. McDougall, S. M. Wright, and A. Han, "A Magnetic Resonance (MR) Microscopy System Using a Microfluidically Cryocooled Planar Coil," *Lab on a Chip,* vol. 11, pp. 2197-2203, 2011.

[62]   A. Webb, "True MR Microscopy on a 7 Tesla Scanner: Application to Plaque Detection in Ex Vivo HCHWA-D Samples," in *The International Society for Magnetic Resonance in Medicine*, Honolulu, USA, 2009.

[63]   D. I. Hoult and B. Tomanek, "Use of Mutually Inductive Coupling in Probe Design," *Concepts in Magnetic Resonance,* vol. 15, pp. 262-285, 2002.

[64]   S. M. Wright, "Estimation of the Signal-to-Noise Loss due to Inductive Coupling Loops," in *8th Annual Meeting of the Society of Magnetic Resonance in Medicine*, Amsterdam, The Netherlands, 1989, p. 955.

[65]   S. M. Wright, R. L. Magin, and J. R. Kelton, "Arrays of Mutually Coupled Receiver Coils: Theory and Application," *Magnetic Resonance in Medicine,* vol. 17, pp. 252-268, 1991.

[66]   M. D. Schnall, C. Barlow, V. H. Subramanian, and J. S. Leigh, "Wireless Implanted Magnetic Resonance Probes for In Vivo NMR," *Journal of Magnetic Resonance,* vol. 68, pp. 161-167, 1986.

[67]   A. Raad and L. Darrasse, "Optimization of NMR Receiver Bandwidth by Inductive Coupling," *Magnetic Resonance Imaging,* vol. 10, pp. 55-65, 1992.

[68]   M. A. Ohliger, P. Ledden, C. A. McKenzie, and D. K. Sodickson, "Effects of Inductive Coupling on Parallel MR Image Reconstructions," *Magnetic Resonance in Medicine,* vol. 52, pp. 628-639, 2004.

[69]   D. Sakellariou, G. L. Goff, and J. F. Jacquinot, "High-resolution, High-sensitivity NMR of Nanolitre Anisotropic Samples by Coil Spinning," *Nature,* vol. 447, pp. 694-697, 2007.

[70]   M. Utz and R. Monazami, "Nuclear Magnetic Resonance in Microfluidic Environments Using Inductively Coupled Radiofrequency Resonators," *Journal of Magnetic Resonance,* vol. 198, pp. 132-136, 2009.

[71]   D. I. Hoult and R. E. Richards, "The Signal-to-noise Ratio of the Nuclear Magnetic Resonance Experiment," *Journal of Magnetic Resonance,* vol. 24, pp. 71-85, 1976.

[72]   W. E. Kwok and Z. You, "In Vivo MRI Using Liquid Nitrogen Cooled Phased Array Coil at 3.0 T," *Magnetic Resonance Imaging,* vol. 24, pp. 819-823, 2006.

[73]   J. Wosik, K. Nesteruk, M. R. Kamel, F. Ip, L. Xue, A. C. Wright, and F. W. Wehrli, "Cryogenic Varactor-Tuned 4-element Array and Cryostat for μ-MRI of Trabecular Bone in the Distal Tibia," in *The International Society for Magnetic Resonance in Medicine*, Toronto, Canada, 2008, p. 443.

[74]   C. Baltes, N. Radzwill, S. Bosshard, D. Marek, and M. Rudin, "Micro MRI of the Mouse Brain Using a Novel 400 MHz Cryogenic Quadrature RF Probe," *NMR in Biomedicine,* vol. 22, pp. 834-42, Oct 2009.

[75]   SU-8 Permanent Photoresists (Electrical Properties), MicroChem Corp., Newton, MA. [online]. Available: http://www.microchem.com/pdf/SU-8-table-of-properties.pdf

[76]   I. Ida, K. Ito, and Y. Okano, "Accurate Measurement of Small Input Resistances Using a Conventional Network Analyzer," *IEEE Transactions on Antennas and Propagation,* vol. 47, pp. 389-391, 1999.

[77] R. F. Godley, "Investigation of Cryo-Cooled Microcoils for MRI," Master of Science, Electrical Engineering, Texas A&M University, College Station, Texas, USA, 2011.

[78] M. E. Lacey, R. Subramanian, D. L. Olson, A. G. Webb, and J. V. Sweedler, "High-Resolution NMR Spectroscopy of Sample Volumes from 1 nL to 10 µL," *Chemical Reviews,* vol. 99, pp. 3133-3152, 1999/10/01 1999.

[79] J. E. Stocker, T. L. Peck, A. G. Webb, M. Feng, and R. L. Magin, "Nanoliter Volume, High-resolution NMR Microspectroscopy Using a 60-µm Planar Microcoil," *IEEE Transactions on Biomedical Engineering,* vol. 44, pp. 1122-1127, 1997.

[80] J. D. Trumbull, I. K. Glasgow, D. J. Beebe, and R. L. Magin, "Integrating Microfabricated Fluidic Systems and NMR Spectroscopy," *IEEE Transactions on Biomedical Engineering,* vol. 47, pp. 3-7, 2000.

[81] V. Badilita, B. Fassbender, K. Kratt, A. Wong, C. Bonhomme, D. Sakellariou, J. G. Korvink, and U. Wallrabe, "Microfabricated Inserts for Magic Angle Coil Spinning (MACS) Wireless NMR Spectroscopy," *PLoS One,* vol. 7, p. e42848, 2012.

[82] K. Ehrmann, M. Gersbach, P. Pascoal, F. Vincent, C. Massin, D. Stamou, P. A. Besse, H. Vogel, and R. S. Popovic, "Sample Patterning on NMR Surface Microcoils," *Journal of Magnetic Resonance,* vol. 178, pp. 96-105, 2006.

[83] R. R. A. Syms, M. M. Ahmad, I. R. Young, D. J. Gilderdale, and D. J. Collins, "Microengineered Needle Micro-coils for Magnetic Resonance Spectroscopy," *Journal of Micromechanics and Microengineering,* vol. 16, p. 2755, 2006.

[84] A. G. Goloshevsky, J. H. Walton, M. V. Shutov, J. S. de Ropp, S. D. Collins, and M. J. McCarthy, "Development of Low Field Nuclear Magnetic Resonance Microcoils," *Review of Scientific Instruments,* vol. 76, pp. 024101-6, 2005.

[85] L. Renaud, M. Armenean, L. Berry, P. Kleimann, P. Morin, M. Pitaval, J. O'Brien, M. Brunet, and H. Saint-Jalmes, "Implantable Planar RF Microcoils for NMR Microspectroscopy," *Sensors and Actuators A: Physical,* vol. 99, pp. 244-248, 2002.

[86] L. Ciobanu, D. A. Seeber, and C. H. Pennington, "3D MR Microscopy with Resolution 3.7 μm by 3.3 μm by 3.3 μm," *Journal of Magnetic Resonance,* vol. 158, pp. 178-182, 2002.

[87] V. Badilita, R. C. Meier, N. Spengler, U. Wallrabe, M. Utz, and J. G. Korvink, "Microscale Nuclear Magnetic Resonance: A Tool for Soft Matter Research," *Soft Matter,* vol. 8, pp. 10583-10597, 2012.

[88] C. L. Goldsmith, A. Malczewski, Z. J. Yao, S. Chen, J. Ehmke, and D. H. Hinzel, "RF MEMs Variable Capacitors for Tunable Filters," *International Journal of RF and Microwave Computer-Aided Engineering,* vol. 9, pp. 362-374, 1999.

[89] J. J. Carr, *Secrets of RF Circuit Design*. New York, San Francisco, Washington, D.C.: McGraw-Hill, 2001.

[90] A. D. Helfrick, *Q Factor Measurement*: CRC Press LLC, 2000.

[91] J. I. Seeger and B. E. Boser, "Dynamics and Control of Parallel-Plate Actuators beyond the Electrostatic Instability," in *Transducers '99, The 10th International Conference on Solid-State Sensors and Actuators*, Sendai, Japan, 1999, pp. 474-477.

[92]   J. I. Seeger and B. E. Boser, "Charge Control of Parallel-plate, Electrostatic Actuators and the Tip-in Instability," *Journal of Microelectromechanical Systems,* vol. 12, pp. 656-671, 2003.

[93]   M. Bakri-Kassem and R. R. Mansour, "High Tuning Range Parallel Plate MEMS Variable Capacitors with Arrays of Supporting Beams," in *19th IEEE International Conference on Micro Electro Mechanical Systems*, Istambul, Turkey, 2006, pp. 666-669.

[94]   L. Kogut, "The Influence of Surface Topography on the Electromechanical Characteristics of Parallel-plate MEMS Capacitors," *Journal of Micromechanics and Microengineering,* vol. 15, p. 1068, 2005.

[95]   J. Zou, C. Liu, and J. E. Schutt-Ainé, "Development of a Wide-tuning-range Two-parallel-plate Tunable Capacitor for Integrated Wireless Communication Systems," *International Journal of RF and Microwave Computer-Aided Engineering,* vol. 11, pp. 322-329, 2001.

[96]   F. Zhiping, Z. Wenge, S. Bingzhi, K. F. Harsh, K. C. Gupta, V. Bright, and Y. C. Lee, "Design and Modeling of RF MEMS Tunable Capacitors Using Electro-thermal Actuators," in *IEEE MTT-S International Microwave Symposium*, Anaheim, USA, 1999, pp. 1507-1510.

[97]   Z. Jun, L. Chang, J. Schutt-Aine, C. Jinghong, and K. Sung-Mo, "Development of a Wide Tuning Range MEMS Tunable Capacitor for Wireless Communication Systems," in *International Electron Devices Meeting*, San Francisco, USA, 2000, pp. 403-406.

[98]   J. Y. Park, Y. J. Yee, H. J. Nam, and J. U. Bu, "Micromachined RF MEMS Tunable Capacitors Using Piezoelectric Actuators," in *IEEE MTT-S International Microwave Symposium*, Phoenix, USA, 2001, pp. 2111-2114.

[99]   R. L. Borwick, III, P. A. Stupar, J. F. DeNatale, R. Anderson, and R. Erlandson, "Variable MEMS Capacitors Implemented Into RF Filter Systems," *IEEE Transactions on Microwave Theory and Techniques,* vol. 51, pp. 315-319, 2003.

[100]   A. Abbaspour-Tamijani, L. Dussopt, and G. M. Rebeiz, "Miniature and Tunable Filters Using MEMS Capacitors," *IEEE Transactions on Microwave Theory and Techniques,* vol. 51, pp. 1878-1885, 2003.

[101]   R. Mahameed and G. M. Rebeiz, "Electrostatic RF MEMS Tunable Capacitors with Analog Tunability and Low Temperature Sensitivity," in *IEEE MTT-S International Microwave Symposium*, Anaheim, USA, 2010, pp. 1254-1257.

[102]   S.-J. Chen, C.-Y. Lee, and E. S. Kim, "Integration of Piezoelectric Tunable Capacitors and Bonded-wire Inductors for Contactless RF Switch and Tunable Filter," *Sensors and Actuators A: Physical,* vol. 165, pp. 73-78, 2011.

[103]   D. T. McCormick, L. Zhihong, and N. Tien, "Dielectric Fluid Immersed MEMS Tunable Capacitors," in *IEEE MTT-S International Microwave Symposium*, Philadelphia, USA, 2003, pp. 495-498.

[104]   S. O. Choi, Y. K. Yoon, M. G. Allen, and A. T. Hunt, "A Tunable Capacitor Using an Immiscible Bifluidic Dielectric," in *IEEE MTT-S International Microwave Symposium*, Fort Worth, USA, 2004, pp. 873-876

[105]   Y. Bai, Z. Y. Cheng, V. Bharti, H. S. Xu, and Q. M. Zhang, "High-dielectric-constant Ceramic-powder Polymer Composites," *Applied Physics Letters,* vol. 76, pp. 3804-3806, 2000.

APPENDIX

1. Protocol

(1) PDMS Soft-lithography

- Mix PDMS pre-polymer (Sylgard 184, Dow corning, Inc.) with curing agent (10:1 w/w)

- Pour the PDMS mixture over the soft-lithography master mold

- Remove bubbles by degassing the PDMS mixture inside a vacuum chamber for 10-30 min

- Place the degassed PDMS inside a leveled 85℃ oven for at least 45 min for polymerization

- Peel off the polymerized PDMS layer from the master mold

(2) Copper Electroplating

- Place a metal plate and your sample at the stand (Do Not change the fixed distance between the plate and sample)

- Connect + wire (red color) of the power supply to the metal plate and − wire (green color) of the power supply to your sample
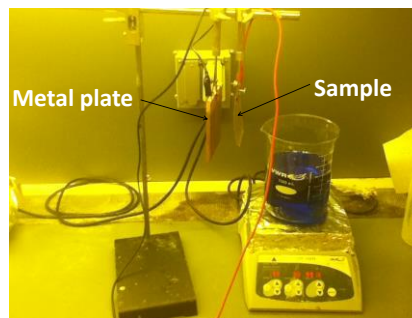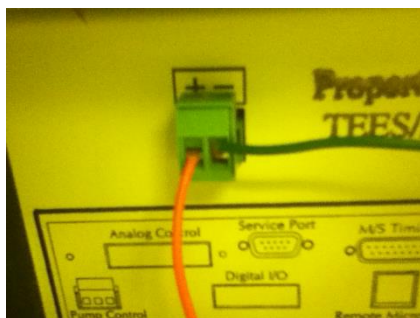
- Place a beaker on the hotplate and pour electroplating solution and put a magnetic bar to stir the solution (Set the stirrer speed at 90 RPM)

- Turn on the power supply

- Set the total run time

- Set the current (using the density of 10 mA/cm^2)

- To run the electroplating, press OPR button.

- If the displayed voltage is high and the displayed current is 0.001, it means there is no current flow. Check the electric wire connection and your sample.

- If you want to pause or stop the electroplating, press STBY button.

- Once the run is over, press STBY button and turn off the power supply

- Take out the metal plate and your sample. Wash them with DI water and dry them with N_2 gas.

- Pour the electroplating solution into the container and rinse the beaker with DI water

- Clean out the area you used.

2. COMSOL simulation

Open

1. Open COMSOL by double-clicking its icon. When the "Model Wizard" opens, select a space dimension: 2D (or 3D).
2. In the "Add physic" window, click the heat transfer folder, then click "heat transfer in solid". Click the next arrow button.
3. In the "Select study type" window, click to select stationary study type. (or time dependent). Then click the finish button.
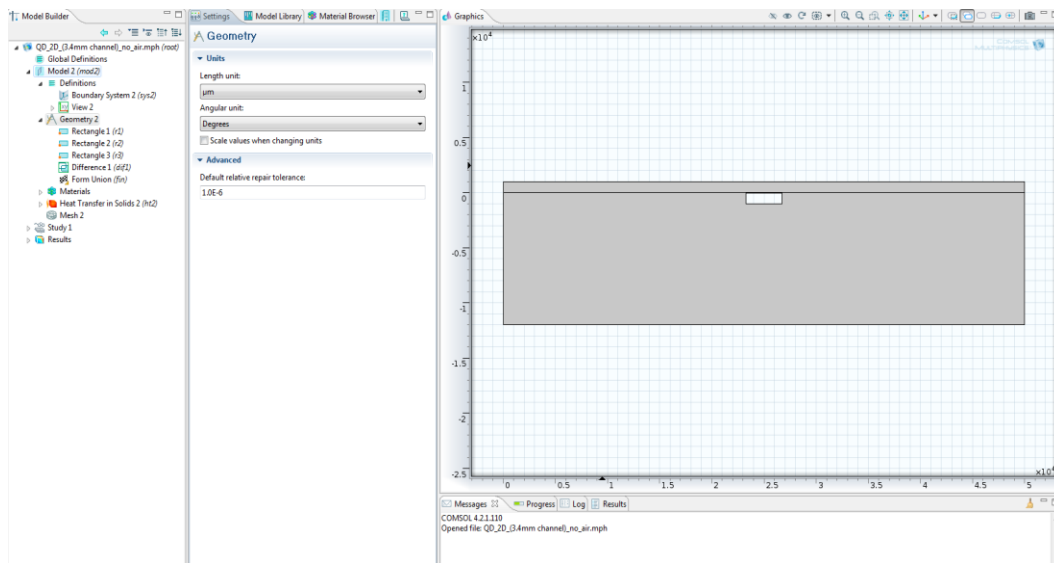4. Click "Geometry1" in the "Model builder" window, and change the length unit to "μm".

Drawing

5. Right-click "Geometry1" in the "Model builder" window, then click "Import" to import DXF file, or click shapes which you want to add.
6. To draw a cryo-channel device consisting of a glass sheet and a cryo-channel embedded PDMS , click "rectangle" and enter the value of Width, 50000 μm, Height, 1000 μm, x, 0 μm, and y, 0 μm. Right-click "Geometry1" and click "rectangle" and enter the value of Width, 50000 μm, Height, 12000 μm, x, 0 μm, and y, -12000 μm. Add a rectangle again and enter the value of Width, 3400 μm, Height, 1000 μm, x, 23300 μm, and y, -1030 μm

7. To define the cryo-channel, right-click "Geometry1" and select "Boolean operations" =>
"Difference".

8. In the "Difference" window, click the "Objects to add" and click the largest rectangle (r2)
in the "Graphics" window. Then click "+" button to add to selection.

9. In the "Difference" window, click the "Objects to subtract" and click the smallest
rectangle (r3) in the "Graphics" window. Then click "+" button to add to selection.

Materials

10. In the "Model builder" window, right-click "Materials" and select "Open Material
Browser"

11. In the "Material Browser", expand the "Built-in" folder, locate Air, right-click and select
"Add Material to Model"

12. To add new material like PDMS, right-click "Materials", select "Material", right-click
the generated "Material A1" and rename it as "PDMS"

13. To add material properties, click the "PDMS" under the material folder, expand
"Material Properties" in the "Material" window. Click "Basic properties" and right-click the
property which you want to add and select "add to material".

Table A1. Example of PDMS and soda lime glass properties for the heat transfer simulation. (These values are not absolute values. You can find a range of values.)

	Thermal Conductivity	Density	Heat capacity
PDMS	0.17 W/(m*K)	965 kg/m^3	1500 J/(kg*K)
Soda lime glass	0.94 W/(m*K)	2440 kg/m^3	657 J/(kg*K)

14. Click "PDMS" under the material folder in the "Model builder", select the largest domain in the "Graphics" window using left-click, and right-click to add the selection.

15. Add "Soda lime glass" material using same procedure. Then Click "Soda lime glass", select the thin rectangle in the "Graphics" window using left-click, and right-click to add the selection.
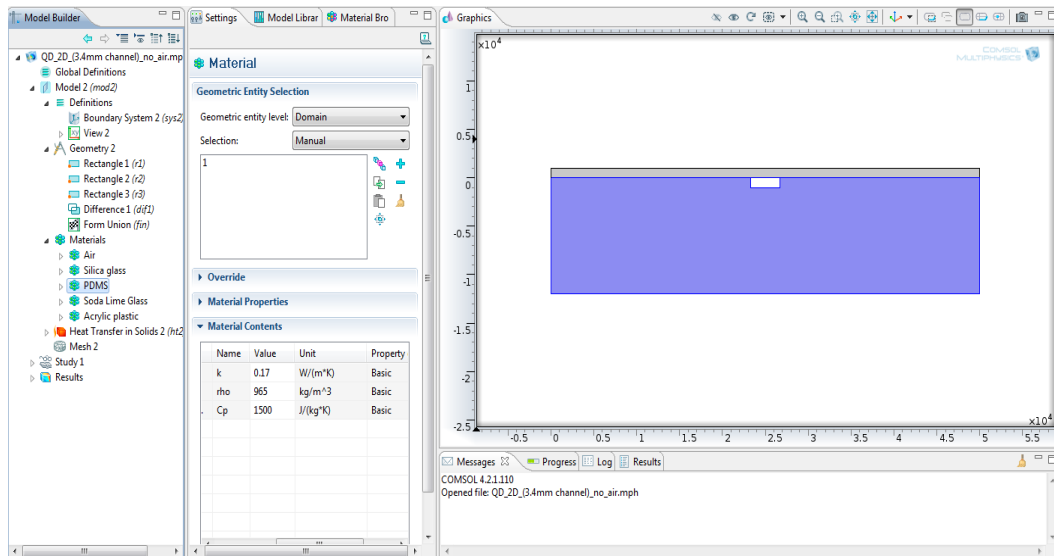

Physics

16. In the "Model Builder", expand the "Heat Transfer in Solid" node.

17. Select "Initial Values1" and enter the value of 293.15K in the "Temperature" in the "Initial Values" window.

18. Right-click the "Heat Transfer in Solid" in the "Model Builder", click "Temperature" and "Heat flux"

19. Click the added "Temperature" under "Heat Transfer in Solid", and select the four walls inside the PDMS in the "Graphics". Enter 77K (Liquid nitrogen temperature) in the "Temperature" window.
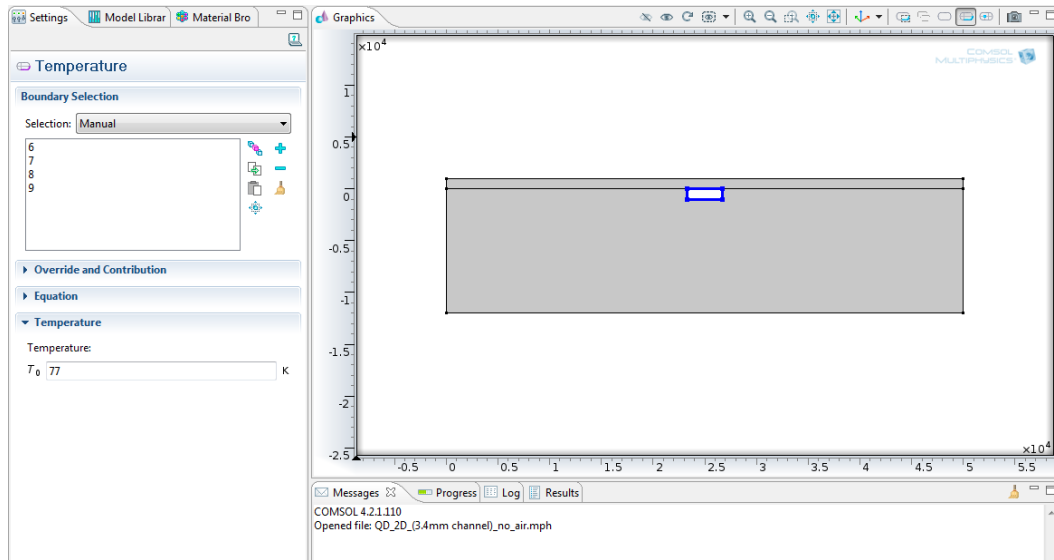

20. Click the added "Heat flux" under "Heat Transfer in Solid", and select the outside walls of the whole device in the "Graphics". Select "Inward heat flux" in the "Heat flux" window and enter 10 W/(m^2*K) as the heat transfer coefficient and enter 293.15K as the external temperature.

With regard to typical values of heat transfer coefficient, choose 3 to 20 W/(m^2*K) if the experiment situation is free convection in air and use 10 to 200 W/(m^2*K) if the situation is under the forced convection in air.
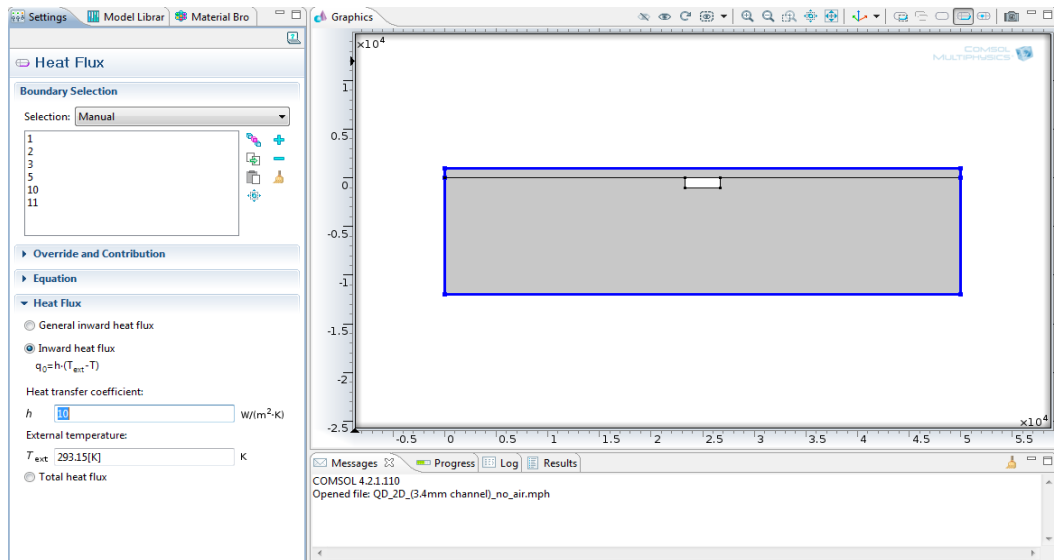
Mesh

21. Click "Mesh" In the "Model Builder", select "Element size". Click the "Build all" button

in the "Size settings" window to create the mesh as show in this figure.
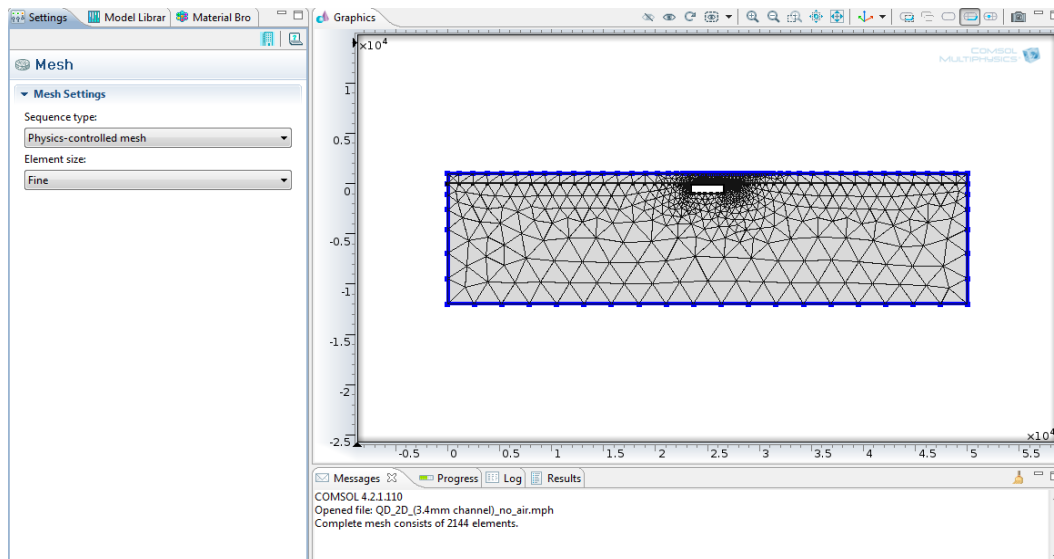
Study

22. To run a simulation, right-click "study I" in the "Model Builder" and choose "Compute".

Results

23. Under "Results"=>"Temperature", click the "Surface1". In the "Settings" window, click "Range" and select "Manual color range" to see the interesting part in the result image.

24. To see the temperature gradient using contour, click the "contour" under "Isothermal Contours".